Available online at www.sciencedirect.com
SCIENCE DIRECT®
Physica A 346 (2005) 217–249
PHYSICA A
www.elsevier.com/locate/physa

On axisymmetric creeping flows involving a hybrid droplet

D. Palaniappan, Prabir Daripa*

Department of Mathematics, Texas A&M University, College Station, Texas, TX 77843-3368, USA

Available online 11 September 2004

Abstract

The Stokes flow involving a hybrid droplet submerged in an immiscible liquid is considered. The droplet has a two-sphere geometry with the two spherical surfaces intersecting orthogonally. The types of hybrid droplet considered here include (i) vapor–solid; (ii) vapor–vapor; and (iii) vapor–liquid, with the first two being limiting cases of (iii). It is assumed that the surface tension is sufficiently large so that the interfaces have uniform curvature. In a constructive and simple manner, steady state solutions of Stokes equations involving such configurations are constructed.

The theory leading to the general expressions for the flow fields under the above-mentioned limitations exploit the inverse transformation, and the reflection and translation properties of the axisymmetric biharmonic function associated with the Stokes flow. These are cast in the form of a theorem followed by a simple proof. The theorem is then applied to construct closed form singularity solutions for several axisymmetric flow fields disturbed by a hybrid droplet. The different primary flow fields considered here include paraboloidal flow, flow due to a, single stokeslet and a pair of stokelets, and flow due to a potential-dipole. The salient features of the image singularities are discussed in each case. In all cases, the drag force is found to vary significantly with respect to the two radii associated with the two-sphere geometry of the droplet, and the viscosity ratio of the two liquids in the continuous and dispersed phases. In the case of singularity driven flows, the drag is influenced by an additional parameter namely, the location of the singularity. The flow streamlines in some cases show interesting flow patterns. In the case of paraboloidal flows, either a single eddy or a pair of eddies is observed depending on the ratio of the two radii. The sizes and shapes of these eddies vary monotonically with viscosity ratio. For flows due to a single and a pair of stokeslets with the

*Corresponding author. Tel.: +1-409-845-1204; fax: +1-409-845-4190.
E-mail address: daripa@math.tamu.edu (P. Daripa).

0378-4371/$ - see front matter
doi:10.1016/j.physa.2004.08.014

same strength, no eddy is noticed. However, a toroidal eddy appears in the case of a pair of stokelets with opposite strengths. The locations of the stokeslets and the viscosity ratio influence the eddy structure significantly.

PACS: 47.15.Gf

Keywords: Creeping flows; Hybrid droplet; Paraboloidal flows; Stokeslet; Point-source doublet; Potential-dipole

1. Introduction

In this paper, we investigate general axisymmetric flows associated with a hybrid drop consisting of a vapor–solid/vapor–vapor/vapor–liquid configuration with an interior spherical interface separating the two phases. The vapor–liquid droplet represents a more general family of hybrid configurations of which vapor–solid and vapor–liquid droplets are limiting cases. Therefore, we provide a detailed analysis for the vapor–liquid droplet which leads to the results for the limiting cases. The vapor–liquid hybrid droplet has a two-sphere geometry (see Fig. 1): one spherical surface is the interface between the vapor and the liquid of the continuous phase, and the other spherical surface is the interface between the dispersed and continuous phase liquids. The vapor–liquid hybrid droplet is also called a partially encapsulated droplet or a two-sphere assembly.

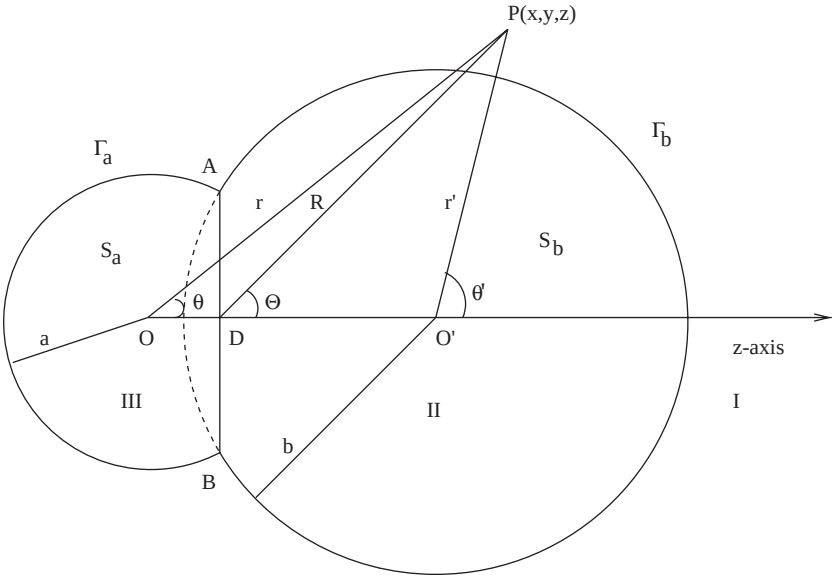

Fig. 1. Schematic of a vapor–liquid hybrid droplet Γ.

We derive general formulas for calculating the flow fields in the continuous and the dispersed phases under following conditions. Firstly, for simplicity, two spherical surfaces of the two-sphere assembly are assumed to intersect at an angle $\frac{\pi}{2}$. This assumption may appear very special, but we see the present effort as an important and useful extension of the extensive works on the hydrodynamics of spherical particles.

While the subject of partially encapsulated drops has attracted the attention of many workers, general study of this problem even with constraints like the one mentioned above has not been carried out. The main reason could be that the mathematical tools for handling such geometrical surfaces have not been available. The theoretical analysis under this assumption leads to exact closed form solutions for various axisymmetric flows for the drop-bubble case. In this paper, we present these results and interesting flow features that we have discovered through numerical experiments in parameter space. These flow features in themselves are sufficient enough to warrant their presentation which is one of the things, among others, that we do in this paper. Before going over to the detailed analysis and numerical results, we provide a few other motivating factors.

Partially engulfed drops are encountered in many suspensions. The rheological and dynamic behavior of suspensions of non-spherical particles encompass a much richer class of phenomena than that exhibited by suspensions of spheres. Studies of model suspensions of spheroids [1,2] have elucidated the role of hydrodynamic forces on the alignment and arbitrary distribution, and consequently on the bulk rheology. Indeed, hybrid drops occur in processes such as melting of ice particles in the atmosphere, liquid membrane technology, as well as in other industrial operations. Such drops are also found to exist in lipid bilayer [3] and polymer grafted [4] membranes in concentrated solutions. A comprehensive literature on hybrid drops may be found in Johnson et al. [5] and Sadhal et al. [6]. In electrostatics, it is common to model certain hybrid (merging) objects as two intersecting spherical surfaces to study their responses to applied electric fields [7,8]. This model has also been used in the electric field-induced cell-to-cell fusion process to predict the fusion of biological cells [9]. In those studies, modeling by the use of Laplace equation was adequate and provided excellent theoretical results. In viscous hydrodynamics, however, flows in and around such hybrid objects which are governed by biharmonic equation, instead of Laplace equation, have not been studied adequately so far and still remain challenging.

Most of the models that incorporate non-sphericity (ranging from disks to needles) may be viewed as degenerate ellipsoids, whereas the overlapping configurations do not belong to this category. Not surprisingly, the models with ellipsoids and spheroids have received more attention than the models with overlapping spheres. Earlier works involving hybrid drops have dealt with very few special unbounded flows [10–12]. However, it is advantageous to have general formulas, if possible, and use them to explore various flow features. Such general formulas are obtained in this paper by the method of images when the spheres intersect at a contact angle $\frac{\pi}{2}$.

Another motivation for the present work originates from issues raised by several workers on the singularity method for Stokes flows. This method, developed by Lorentz [13], has been applied by many to solve fluid motion around non-spherical objects and Chwang and Wu [14] developed it further and reviewed previous works (see also Refs. [15,16]). The essence of those works is that for a surprisingly large class of problems, the disturbance velocity fields produced by spheroids and ellipsoids may be constructed from rather simple distributions of fundamental singularities (Green's functions) over a line or ellipse, respectively. The types and domains of distribution of singularity required for solving various boundary value problems have been obtained by direct evaluation by various authors. An interesting observation for flows past a fixed shape is that only the type of singularities, and not the domain of distribution of the singularities, depends on the flows in the far-field. There are two main drawbacks with this singularity method. First, it does not reveal whether a simple singularity solution exists. Second, it does not provide an ab initio procedure for determining the locations of the image singularities.

We present here solutions for flows in and around a hybrid drop suspended in arbitrary axisymmetric flows in a form similar to that provided by Lorentz [13] (see also [17]) for plane wall. Our general results provide not only the solutions in singularity forms but also the types and locations of the image singularities for each prescribed unbounded flow. It has been observed in the literature that for spheroids, the region of distribution of image singularities is the line between the foci [14] and for ellipsoids it is the confocal ellipse [15]. In contrast, for hybrid drops it turns out that the image singularities are located at three points inside the two-sphere assembly, if the two spheres intersect orthogonally. The generalization for other contact angles eludes us at this moment, but our approach offers hints that will be pursued in our future work.

The paper is organized as follows. In Section 2, the two-sphere geometry of a hybrid droplet of various types and surface tension forces on the surface of this hybrid droplet are discussed. Section 3 starts with the statement of the problem using velocity and pressure fields. Since we are concerned with axisymmetric flow fields, it is convenient to use stream function formulation. Therefore, the problem is reformulated and the boundary and interface conditions are expressed in terms of the stream function. The axisymmetric biharmonic equation satisfied by the stream function possesses some nice properties. By the use of cylindrical coordinates, these simple properties are narrated for later reference. The key steps in the solution procedure consists of successive reflections (three times) of the given flow field. For the sake of clarity, these major steps based on the method of reflection are discussed in the same section.

Our main results of the present work appear in Section 4. The general solutions for the stream functions in the continuous and dispersed phases are provided in closed form. These formulas are presented in the form of a theorem followed by a simple proof. In Section 5, the utility of our general results are demonstrated for several choices of free-stream flows. The image system, the location of the image singularities and their strengths are interpreted in each case. It turns out that the image singularities for free-stream flows are located at the centers of the two spheres

and at their common inverse point. For singularity driven flows (stokeslet, dipole, etc.), the location of the primary singularity dictates the location of the image singularities. Furthermore, the stokeslet solution is applied to compute an approximate drag on a particle located outside the hybrid droplet. In Section 6, we conjecture a Faxen-type relation for drag force on the hybrid droplet in any arbitrary axisymmetric flows. In Section 7, the flow fields are sketched for different flows considered in Section 5 because of interesting flow patterns. The features of these streamline patterns are also discussed in detail in the same section. The main findings of the present study are summarized in the concluding Section 8.

2. Geometry of the hybrid droplet

The two-sphere geometry of the hybrid droplet is depicted in Fig. 1. This geometry consists of two unequal overlapping spheres S_a and S_b of radii a and b with centers at O and O' respectively. We assume that these spheres intersect orthogonally. The boundary of the droplet is denoted by $\Gamma = \Gamma_a \cup \Gamma_b$, where Γ_a is part of the boundary where $r = a$ and Γ_b is part of the boundary where $r = b$ (see Fig. 1). Since the spheres overlap at a contact angle $\pi/2$, the two centers share a common inverse point D. In the right-angled triangle OAO', $c^2 = a^2 + b^2$, where $OO' = c$. In the meridian plane, the line AB intersects OO' at D. Hence, $OD = a^2/c$ and $DO' = b^2/c$. Let (r, θ, ϕ), (r', θ', ϕ) and (R, Θ, ϕ) be the spherical polar coordinates of any point outside the assembly Γ with origins O, O' and D respectively. Then following geometrical relations are evident from Fig. 1:

$$r^2 = r'^2 + 2cr' \cos\theta' + c^2 , \tag{1}$$

$$r'^2 = r^2 - 2cr \cos\theta + c^2 , \tag{2}$$

$$\begin{aligned} R^2 &= r^2 - 2\frac{a^2}{c} r \cos\theta + \frac{a^4}{c^2} \\ &= r'^2 + 2\frac{b^2}{c} r' \cos\theta' + \frac{b^4}{c^2} . \end{aligned} \tag{3}$$

We see from Eqs. (1)–(3) that on the spheres S_a and S_b, r' and r reduce to

$$r' = \frac{c}{a} R \quad \text{on } r = a , \tag{4}$$

$$r = \frac{c}{b} R \quad \text{on } r' = b . \tag{5}$$

The three types of hybrid droplet are as follows:

(i) *Vapor–Solid*: Part of the sphere S_a is vapor and part of the sphere S_b is a solid. In this case, hybrid droplet is perhaps a misnomer, but we use this for this type also because this is a limiting case of type (iii) hybrid droplet discussed below.

(ii) *Vapor–Vapor*: Part of the sphere S_a is vapor and part of the sphere S_b is also vapor.
(iii) *Vapor–liquid*: Part of the sphere S_a is vapor and part of the sphere S_b contains a liquid with viscosity different from the viscosity of the ambient liquid.

It may be noted that the types (i) and (ii) are limiting cases of type (iii). Therefore, we describe our analysis for a vapor–liquid hybrid droplet (type (iii)) and indicate how the results for (i) and (ii) can be obtained from the general results.

As mentioned above, in the vapor–liquid hybrid configuration, part of the sphere S_a contains vapor and part of the sphere S_b contains a liquid with viscosity different from the viscosity of the liquid around the droplet. The (spherical) interface between the phases is assumed to have a (unspecified) uniform curvature and is determined as part of the solution (see Section 4.1). It should be remarked that the line AB shown in Fig. 1 is the projection of the plane of intersection of the two spheres S_a and S_b on the meridian plane and it should not be confused with the spherical interface between the phases inside the hybrid droplet.

We designate the fluid region exterior to Γ as I and the spherical regions S_b and S_a as II and III respectively. The surface tension forces are assumed to be large enough to keep the interfaces in a spherical shape. The vapor–liquid configuration exists at rest with contact angle approximately 90° if $\gamma_{I,II} \approx \gamma_{II,III} \gg \gamma_{I,III}$ which is in agreement with the Laplace law on all interfaces. Here the $\gamma_{a,b}$ denotes the capillary pressure at the interface separating regions a and b.

The assumption of $\pi/2$ contact angle, even though a necessity here to make analytical progress, is a first step towards solving the problem for arbitrary contact angle, perhaps through some perturbation techniques or numerical methods. The solution provided here can also be very useful for validation of many numerical methods and codes which attempt to solve such complex problems computationally. The solution can also be useful in many practical situations where this may serve as a good approximation. For instance, in the phenomena of 'two drops glued together' that occurs in three-phase emulsions, in direct-contact heat exchange between two-immiscible liquids and in separation technology where drops and bubbles are used to capture particulate impurities (see Ref. [6]).

3. Formulation of the problem

We consider a stationary hybrid drop submerged in an arbitrary axisymmetric flow of a viscous fluid. Below, the continuous phase means the exterior of the hybrid droplet, while dispersed phase means the interior region. The Reynolds number of the flow fields is assumed to be small so that all inertial effects are negligible. In this case, the governing equations for fluid flow are the linearized steady Navier–Stokes equations, also called creeping flow equations or Stokes equations,

$$\mu^{(i)}\nabla^2\mathbf{q}^{(\mathbf{i})} = \nabla p^{(i)}, \quad \nabla\cdot\mathbf{q}^{(\mathbf{i})} = 0\,, \tag{6}$$

where $i = 1, 2$ is used to denote continuous and dispersed liquid phases respectively, $\mathbf{q}^{(\mathbf{i})}, p^{(i)}$ and $\mu^{(i)}$ are the velocities, pressures and viscosities in the respective phases. The boundary and interface conditions are as follows:

- Velocity and pressure far from the droplet are that of a specified basic flow:

$$\mathbf{q} \to \mathbf{q}_0, \quad p \to p_0 \quad \text{as } r \to \infty ,$$

  where $r = \sqrt{x^2 + y^2 + z^2}$.
- Zero normal velocity on Γ:

$$\mathbf{q} \cdot \hat{\mathbf{n}}_a = \mathbf{q} \cdot \hat{\mathbf{n}}_b = 0, \quad \text{on } \Gamma ,$$

  where $\hat{\mathbf{n}}_a$ and $\hat{\mathbf{n}}_b$ are unit normals at the spherical surfaces S_a and S_b respectively.
- Continuity of tangential velocity and shear stress at the liquid–liquid interface Γ_b:

$$q_t^{(1)} = q_t^{(2)}, \quad \tau_t^{(1)} = \tau_t^{(2)} \quad \text{on } \Gamma_b ,$$

  where $q_t^{(i)}$ and $\tau_t^{(i)}$ are the tangential components of the velocity and surface force respectively.
- Zero shear-stress at the vapor–liquid interface Γ_a:

$$\tau_t^{(1)} = 0 \quad \text{on } \Gamma_a .$$

As we will see below, the solution of the governing Stokes equations (6) subject to the above mentioned far-field and interface conditions provides the velocities and the pressures in the dispersed and continuous phases prevailing in the presence of the hybrid droplet and also the topology of the interior (drop-bubble) interface. In fact, we will see (see note 3 at the end of Section 4.1) that the solution to the above problem gives the interior drop-bubble interface as the extension of larger spherical surface in the interior of the hybrid geometry, i.e., the dashed curve in Fig. 1. The solutions are obtained by ignoring the normal stress condition at all the interfaces as normal stress imbalance is likely to cause a slight deformation of the interfaces assuming very high surface tension.

The tangential stress condition at the interior interface has been ignored because the non-zero tangential stress will not disturb the rotational equlibrium of the configuration due to symmetry of the configuration about the x-axis (see Fig. 1). Moreover, the non-zero tangential stress will cause very slight deformation assuming very high viscous fluid inside the droplet when the velocity gradients at the interface will be negligibly small to offset the multiplicative effect of the high viscosity coefficient in the tangential stress term. Thus the solutions given are certainly valid to a first approximation assuming extremely high viscosity of the interior fluid and low capillary number.

It should be noted here that the issue of the dynamic boundary conditions at the interior drop-bubble interface AB (Fig. 1) does not arise if Γ is a vapor–solid droplet ($\mu^{(2)} \to \infty$) or a vapor–vapor droplet ($\mu^{(2)} \to 0$). In the vapor–solid case, the velocity in the dispersed phase becomes zero since there is no fluid in region II and the tangential stress $\tau^{(2)}$ does not exist. In the vapor–vapor case with no interior motion, no interface condition on the segment AB is required since this segment is really

irrelevant. Therefore, in these limiting cases, the solutions presented are exact and satisfy all relevant boundary conditions. Only in the vapor–liquid case, the solutions presented are accurate enough when surface tension is high and interior fluid is highly viscous. However, these solutions can be exact if the neglected interface conditions as mentioned in the above two paragraphs can be satisfied by allowing surface tension to vary along these interfaces, e.g. by doping these interfaces with surfactants. In this regard, following three remarks are made here.

- Surfactants on the free interfaces take care of the normal stress imbalance. For example, the jump in normal stress across the drop-bubble interface must be balanced by the capillary force, T, given by

$$T_{(\gamma_{II,III})} = [-p_{vapor} - \tau^{(2)}_{r'r'}]_{r'=b}\,, \tag{7}$$

  where $T_{(\gamma_{II,III})}$ denotes the capillary force, p_{vapor} is the pressure inside the bubble, and

$$\tau^{(2)}_{r'r'} = -p^{(2)} + 2\mu^{(2)}\,\frac{\partial q^{(2)}_{r'}}{\partial r'}$$

  is the normal stress in the dispersed fluid region. This condition implies that surface tension will have to vary along the drop bubble interface which is possible only if the interface is selectively doped with surfactant such that the above condition is satisfied. In this sense, this configuration can only be realized perhaps under controlled mechanisms. This limitation, however, may be eliminated if the interface is allowed to take any shape in accordance with (7). In this case, the analysis can become quite cumbersome and falls outside the scope of this paper. However, for the sake of completeness, we have provided the expression for the capillary force T given in (7) for each flow field discussed later in Section 5.
- It is assumed that the associated Marangoni traction due to variable surface tension on the exterior free surfaces (Γ_a, Γ_b) is negligible; and
- Associated Marangoni traction on the internal interface along with some controlled mechanisms, if necessary, perhaps can annihilate the tangential stress imbalance on this interface.

Now, we continue the formulation of the problem. The axial symmetry of the flow about z-axis suggests use of the Stokes stream function formulation which requires the solution of the fourth-order scalar equation

$$L^2_{-1}\psi = 0\,, \tag{8}$$

where L_{-1} is the axisymmetric second-order Stokes operator given by

$$\begin{aligned} L_{-1} &= \frac{\partial^2}{\partial r^2} + \frac{1-\eta^2}{r^2}\,\frac{\partial^2}{\partial \eta^2} \\ &= \frac{\partial^2}{\partial r'^2} + \frac{1-\eta'^2}{r'^2}\,\frac{\partial^2}{\partial \eta'^2}\,, \end{aligned} \tag{9}$$

for the spherical coordinates (r,θ) with $\eta=\cos\theta$ and (r',θ') with $\eta'=\cos\theta'$ respectively. Now, the velocity components in terms of the stream function are given by

$$q_r^{(i)}=\frac{1}{r^2\sin\theta}\frac{\partial\psi^{(i)}}{\partial\theta} \tag{10}$$

$$q_\theta^{(i)}=-\frac{1}{r\sin\theta}\frac{\partial\psi^{(i)}}{\partial r}\,, \tag{11}$$

and the pressure is obtained from

$$\frac{\partial p^{(i)}}{\partial r}=\frac{\mu^{(i)}}{r^2\sin\theta}\frac{\partial}{\partial\theta}(L_{-1}\psi^{(i)})\,, \tag{12}$$

$$\frac{\partial p^{(i)}}{\partial\theta}=-\frac{\mu^{(i)}}{\sin\theta}\frac{\partial}{\partial r}(L_{-1}\psi^{(i)})\,. \tag{13}$$

The boundary conditions in terms of the stream function become

$$\psi^{(1)}=0=\frac{\partial}{\partial r}\frac{1}{r^2}\frac{\partial\psi^{(1)}}{\partial r}\,, \tag{14}$$

on Γ_a, the part of the droplet where $r=a$, and

$$\psi^{(1)}=0=\psi^{(2)}\,, \tag{15}$$

$$\frac{\partial\psi^{(1)}}{\partial r'}=\frac{\partial\psi^{(2)}}{\partial r'}\,, \tag{16}$$

$$\mu^{(1)}\left(\frac{\partial}{\partial r'}\frac{1}{r'^2}\frac{\partial\psi^{(1)}}{\partial r'}\right)=\mu^{(2)}\left(\frac{\partial}{\partial r'}\frac{1}{r'^2}\frac{\partial\psi^{(2)}}{\partial r'}\right), \tag{17}$$

on Γ_b, the part of the droplet where $r'=b$.

Based on the above formulation, singularity solutions for uniform and some non-uniform flow fields were reported recently in [11] and [12], respectively. By use of a similar technique, we generalize that approach to construct solutions for arbitrary axisymmetric Stokes flows in and around a partially encapsulated droplet. The essential steps involved in the derivation are as follows:

Step 1. Reflect a given flow field ψ_0 on the stress-free sphere S_a and call the perturbation to the given flow as ψ_a.

Step 2. Reflect the given flow field ψ_0 on the fluid sphere S_b and call the perturbation to the given flow as ψ_b.

Step 3. Reflect ψ_a obtained in step 1 in sphere S_b and call the perturbation to ψ_a as ψ_{ab}. Reflecting ψ_b obtained in step 2 in sphere S_a will result in the same stream function, i.e., $\psi_{ab}=\psi_{ba}$.

Hence, the desired solutions are obtained. In first two steps above, we make use of a theorem from [18].

Since the geometry is axisymmetric about z-axis, it is appropriate to use the cylindrical coordinates. Let (ρ, ϕ, z), (ρ', ϕ, z') and (Π, ϕ, Z) denote the cylindrical polar coordinates of a point outside Γ with O, O' and D as origins respectively. The cylindrical and spherical coordinates are related by $\rho = r \sin\theta, z = r\cos\theta$, with similar relations for the coordinates with respect to other origins. The operator $_{-1}$ in cylindrical coordinates, takes the form

$$_{-1} = \frac{\partial^2}{\partial\rho^2} - \frac{1}{\rho}\frac{\partial}{\partial\rho} + \frac{\partial^2}{\partial z^2}\,. \tag{18}$$

Since z does not appear explicitly in the operator L_{-1}, it is form invariant under translation origin along z axis. The following properties are true for Eq. (8):

(A) *Inversion*: If $\psi_0(\rho, z)$ is a solution of (8), then $(\frac{r}{a})^3\psi_0(\frac{a^2}{r^2}\rho, \frac{a^2}{r^2}z)$ is also a solution of (8), where a is the radius of inversion.
(B) *Reflection*: If $\psi_0(\rho, z)$ is a solution of (8), then $\psi_0(\rho, -z)$ is also a solution.
(C) *Translation of origin*: If $\psi_0(\rho, z)$ is a solution of (8), then $\psi_0(\rho, z + h)$, where h is a constant, is also a solution.

4. General solutions

Below, the general expressions for the flow fields in the continuous and dispersed phases are presented in the form of a theorem followed by a simple proof. For the purpose of clarity, the formula for the force acting on the droplet is derived in a separate subsection.

4.1. The theorem

Theorem. Let $\psi_0(\rho, z)$ be the free-space stream function for the axisymmetric motion of a viscous fluid whose singularities lie outside a two-sphere with boundary Γ formed by two generally unequal spherical surfaces intersecting orthogonally, and suppose that $\psi_0(\rho, z) = o(r^2)$ as $r \to 0$. When a hybrid fluid capsule with the dynamic boundary condition relaxed at the interior interface having interface tensions $\gamma_{I,II} \simeq \gamma_{II,III} \gg \gamma_{I,III}$ (see Fig. 1) is introduced in place of the two-sphere geometry in this flow field, the modified stream functions due to the droplet become

$$\begin{aligned}\psi^{(1)}(\rho, z) = \psi_0(\rho, z) &- \frac{r^3}{a^3}\,\psi_0\left(\frac{a^2}{r^2}\,\rho, \frac{a^2}{r^2}\,z\right)\\ &+ \Lambda\left[\left(\frac{r'(r'^2 - 3b^2)}{2b^3} + \frac{r'^2(r'^2 - b^2)}{b^3}\,\frac{\partial}{\partial r'} - \frac{r'^2(r'^2 - b^2)^2}{4b^5}\,L_{-1}r'\right)\Psi\right]\\ &- (1 - \Lambda)\left(-\frac{r'^3}{b^3}\,\Psi\right),\end{aligned} \tag{19}$$

in the continuous phase and

$$\psi^{(2)}(\rho,z) = (1-\Lambda)\frac{(r'^2-b^2)}{2b^2}\left[-3+2r'\,\frac{\partial}{\partial r'}-\frac{(r'^2-b^2)}{2}\,L_{-1}\right]\left(\psi_0(\rho,z)-\frac{r^3}{a^3}\,\psi_0\left(\frac{a^2}{r^2}\,\rho,\frac{a^2}{r^2}z\right)\right), \tag{20}$$

in the dispersed phase. The function Ψ in Eq. (19) is defined as

$$\Psi = \psi_0\left(\frac{b^2}{r'^2}\,\rho', c+\frac{b^2}{r'^2}\,z'\right) - \frac{c^3R^3}{a^3r'^3}\,\psi_0\left(\frac{a^2b^2}{c^2R^2}\,\Pi, \frac{a^2}{c}-\frac{a^2b^2}{c^2R^2}\,Z\right),$$

and $\Lambda = \dfrac{\mu^{(2)}}{\mu^{(1)}+\mu^{(2)}}$.

Note that these solutions correspond to the case of a hybrid fluid capsule (see Fig. 1) which can have discontinuity in shear stress at the interior interface as the dynamic boundary condition on this interior interface has been neglected by construction. It is worth recalling (see end of Section 3) that (Π,ϕ,Z) denote the cylindrical polar coordinates of a point outside Γ with D as the origin.

Proof. The Eqs. (19) and (20) are derived using Steps (1) through (3) (see the text after Eq. (17)) as follows. The second term (let us call it $\psi_a^{(1)}$) on the right-hand side of (19) is the reflection of ψ_0 in the sphere S_a. The reflection of ψ_0 in the fluid sphere S_b, as shown in Ref. [18], leads to a stream function in each of the fluid regions 1 and 2. In region 1, the reflected field is the first term (let us call it $\psi_b^{(1)}$) in the expression for Ψ in (19). In the region 2, the corresponding term is $\psi_0(\rho,z)$ which is in Eq. (20). Likewise, the reflection of $\psi_a^{(1)}$ in the fluid sphere S_b is the last term (which we call $\psi_{ab}^{(1)}$) in the expression for Ψ in (19) for the fluid region 1 and the last term on the right-hand side of (20) for the fluid region 2. Thus $\Psi^{(1)}-\psi_0$ (the perturbation terms in $\psi^{(1)}$ in Eq. (19)) and $\psi^{(2)}$ (given by Eq. (20)) which are solutions of Eq. (8) are obtained by application of properties (A), (B), and (C) for the hybrid-geometry Γ. By a direct verification, it can be seen that $\psi^{(1)}$ and $\psi^{(2)}$ satisfy the boundary conditions (14)–(l7). Since the singularities of ψ_0 lie outside Γ, the singularities of the perturbation terms in $\psi^{(1)}$ will all lie inside Γ. Hence, the perturbed stream function for the continuous phase does not introduce new singularities in the unbounded flow. Finally, since $\psi_0(\rho,z)=o(r^2)$ at the origin, the perturbation terms in (19) are at most of order $o(r)$ for large r. Therefore, the perturbation velocity in the continuous phase tends to zero as $r\to\infty$. This completes the proof. □

Note 1: The functions, $\psi^{(1)}-\psi_0$ (the perturbation terms in $\psi^{(1)}$ in Eq. (19)) and $\psi^{(2)}$ (given by Eq. (20)), are linear in the dimensionless parameter Λ which takes values between zero and one inclusive. For $\Lambda=1$ and $\Lambda=0$ solutions given by Eqs. (19) and (20) reduce to the cases of vapor-rigid hybrid droplet, and vapor–vapor hybrid droplet (composite bubbles) respectively. The complete velocity and pressure fields in the respective phases can be computed using the formulas (10)–(13).

Note 2: Expressions (19) and (20) are in a form similar to the celebrated Lorentz formula [13] for plane wall. The corresponding formulas for a single fluid as well as for a rigid sphere are also available [18–20]. In the limiting case of a single spherical boundary, expressions (19) and (20) reduce to the results found in [18–20].

Note 3: It can be seen from expression (20) that the stream function ψ_2 in the dispersed phase vanishes when $r' = b$ which includes the drop-bubble interface separating the dispersed phase from the vapor, shown as the dashed curve shown in Fig. 1. The fact that the stream function vanishes on this interior interface just says that this is consistent with the assumption on interface tensions, $\gamma_{I,II} \approx \gamma_{II,III} \gg \gamma_{I,III}$, which actually gives the shape of the interior interface.

5. Illustrative examples

In this section, we illustrate the results presented in the previous section by numerous examples. The solutions in the first example has been treated elsewhere [12], and we simply re-derive them by the use of our present formulas. The remaining examples are related to singularity driven flows and are new.

5.1. Paraboloidal flow

The free-space stream function corresponding to axisymmetric paraboloidal flow is $\psi_0 = kp^4$, where k is a constant. The introduction of the hybrid droplet modifies the flow. The perturbed stream functions in the continuous and dispersed phases are obtained readily from (19) and (20) and are given by

$$\begin{aligned}\psi^{(1)}(r,\theta) = {} & K\rho^4 - K\frac{a^5}{r^5}\rho^4 + \Lambda\left[-\frac{7b}{2r'^3}\rho'^2 + \frac{5b^3}{2r'^5}\rho'^2\right. \\ & \left. + \frac{4b}{r'} - \frac{2b^3}{r'^3} - \frac{2r'}{b}\right] K\frac{b^4}{r'^2}\rho'^2 - (1-\Lambda)K\frac{b^5}{r'^5}\rho'^4 \\ & + \Lambda\left[\frac{2a^5b^3}{c^5}R - \frac{8a^5b^5}{c^6}\frac{Z}{R} - \frac{4a^7b^5}{c^7R} + \frac{a^5b^5}{2c^5}\left(7 - 5\frac{b^2}{c^2}\right)\frac{\Pi^2}{R^3}\right. \\ & - \frac{5a^7b^7}{c^8}\frac{\Pi^2 Z}{R^5} - \frac{5a^9b^7}{2c^9}\frac{\Pi^2}{R^5} + \frac{8a^5b^7}{c^7}\frac{Z^2}{R^3} \\ & \left. + \frac{8a^7b^7}{c^8}\frac{Z}{R^3} + \frac{2a^9b^7}{c^9R^3}\right] K\frac{\Pi^2}{R^2} + (1-\Lambda)K\frac{a^5b^5}{c^5}\frac{\Pi^4}{R^5}\,, \end{aligned} \tag{21}$$

for the fluid exterior to the droplet, and

$$\psi^{(2)}(r,\theta) = (1-\Lambda)\frac{(r'^2-b^2)}{2b^2}\left[-3 + 2r'\frac{\partial}{\partial r'} - \frac{(r'^2-b^2)}{2}L_{-1}\right]\left(1 - \frac{a^5}{r^5}\right)K\rho^4\,, \tag{22}$$

for the fluid inside the droplet.

These results are the same as those derived in [12] in spherical coordinates. As discussed there, the image system for the external flow consists of (i) a potential-doublet and a Stokes-quadrupole at O; (ii) stokeslet, potential-doublet, Stokes and potential quadrupoles and potential octupole at O'; and (iii) Stokeslet, Stokes and potential doublets, Stokes and potential quadrupoles and Stokes and potential octupoles at D. The strengths of the image singularities depend on viscosity ratio, radii and the constant k. We discuss the flow patterns in a later section.

The drag on the hybrid droplet suspended in a paraboloidal flow computed from direct integration of stresses (which are derived from stream function given in (21)) over Γ is given by

$$\mathbf{F} = 16\pi\mu^{(1)} k b^3 \Lambda \hat{e}_z \left(1 - \frac{a^5}{c^5}\right), \tag{23}$$

which is in agreement with the expression found in [12]. The discussion on drag in paraboloidal flow has been provided there and it is not reproduced here.

The expression (22) may be used to compute the velocity and pressure in the dispersed phase. The velocity can be calculated using (10), (11) while the pressure may be obtained by integrating (12), (13) after substituting the value for $\psi^{(2)}$ given in (22). The velocity and pressure can then be utilized in (7) to compute the capillary pressure T (see (7)) at the drop-bubble interface. For the sake of brevity, we omit the details and provide here the expression for the imbalance in paraboloidal flow given by

$$T(\gamma_{II,III}) = \left[-p_{vapor} + (1-\Lambda)\mu^{(2)} \frac{2k}{b^2}\left[\frac{\partial}{\partial r'}\left(G + r' \frac{\partial G}{\partial r'}\right) + \frac{2}{\rho'}\frac{\partial G_1}{\partial \theta'}\right]\right]_{r'=b}, \tag{24}$$

where

$$G = \left(4(r'^2 - b^2) - \frac{5}{3}(r'^2 + z'^2)\right) r'z' + 10a^5 \frac{r'}{cr} + 8a^5 \frac{r'z'}{r^3} - a^7\left(\frac{r'}{3cr^3} + \frac{r'}{c}\frac{(z'+c)^2}{r^5}\right),$$

$$G_1 = \rho'^2\left\{5\rho'^2 - 4(r'^2 - b^2) - 5\frac{a^5}{r^3} - 6\frac{a^5 cz}{r^5} - a^5\left[\frac{1}{r^3} + \frac{2cz}{r^5} - a^2\left(\frac{1}{r^5} - \frac{5z^2}{r^7}\right)\right]\right\}.$$

5.2. Stokeslet outside Γ

The problem of finding the flow induced by a stokeslet located outside/inside a rigid spherical container was first solved by Oseen [21] using Green's function approach. This solution of Oseen was used by Higdon [22] to model motion of micro-organisms by flagellar propulsion. Oseen's solution was re-derived later by Shail et al. [23] and by Palaniappan et al. [24] using sphere theorems. Oseen's

solution was further extended to the case of a spherical viscous drop by Fuentes et al. [25] using Lamb's general solution and by Palaniappan et al. [18] using sphere theorems. For a non-spherical geometry, solutions for singularity driven flows have not been obtained to-date. Using the theorem derived in the previous section, we now obtain the solution to the stokeslet problem in the presence of a partially encapsulated droplet.

Consider a stokeslet of strength $\frac{D_3}{8\pi\mu^{(1)}}$, located at a point $(0,0,c+d)$, say E_1, outside Γ. The free-space stream function due to a stokeslet is

$$\psi_0(\rho,z)=\frac{D_3}{8\pi\mu^{(1)}}\frac{\rho_1^2}{r_1}\,, \tag{25}$$

where (ρ_1,z_1) are the cylindrical coordinates with E_1 as origin. The flow fields in the presence of the two-sphere assembly with a stokeslet outside it can be obtained by the use of the theorem presented in Section 4.1. For the continuous phase we obtain

$$\begin{aligned}\psi^{(1)}(\rho,z)=&\frac{D_3}{8\pi\mu^{(1)}}\frac{\rho_1^2}{r_1}-\frac{D_3}{8\pi\mu^{(1)}}\frac{a}{c+d}\frac{\rho_2^2}{r_2}+\frac{D_3}{8\pi\mu^{(1)}}\Lambda\left[-\frac{b}{2d}\left(3-\frac{b^2}{d^2}\right)\frac{\rho_3^2}{r_3}\right.\\&\left.+\frac{b^3(d^2-b^2)^2}{2d^5}\frac{\rho_3^2}{r_3^3}-\frac{b^3(d^2-b^2)}{d^4}\frac{\rho_3^2 z_3}{r_3^3}\right]-\frac{D_3}{8\pi\mu^{(1)}}(1-\Lambda)\frac{b}{d}\frac{\rho_3^2}{r_3}\\&+\frac{D_3}{8\pi\mu^{(1)}}\Lambda\left\{\left[\frac{ab}{2(b^2+cd)}\left(3-\frac{b^2(c+d)^2}{(b^2+cd)^2}\right)\right]\frac{\rho_4^2}{r_4}\right.\\&\left.-\frac{a^3b^3(d^2-b^2)(c+d)}{(b^2+cd)^4}\frac{\rho_4^2 z_4}{r_4^3}-\frac{a^5b^3(d^2-b^2)^2}{2(b^2+cd)^5}\frac{\rho_4^2}{r_4^3}\right\}\\&+\frac{D_3}{8\pi\mu^{(1)}}(1-\Lambda)\frac{ab}{b^2+cd}\frac{\rho_4^2}{r_4}\,,\end{aligned} \tag{26}$$

and for the dispersed phase, we have

$$\begin{aligned}\psi^{(2)}(\rho,z)=&(1-\Lambda)\frac{(r'^2-b^2)}{2b^2}\frac{D_3}{8\pi\mu^{(1)}}\left[-3+2r'\frac{\partial}{\partial r'}-\frac{(r'^2-b^2)}{2}L_{-1}\right]\\&\left(\frac{\rho_1^2}{r_1}-\frac{a}{c+d}\frac{\rho_2^2}{r_2}\right),\end{aligned} \tag{27}$$

where (ρ_2,z_2), (ρ_3,z_3), (ρ_4,z_4) are the cylindrical polar coordinates of a point with E_2,E_3,E_4 as origin, respectively, and r_j is given by

$$r_j^2=r^2-2OO_jr\cos\theta+OO_j^2\quad(j=1,2,3,4)\,. \tag{28}$$

The distances OO_j are $OO_1=c+d$, $OO_2=\frac{a^2}{c+d}$, $OO_3=\frac{b^2+cd}{d}$, $OO_4=\frac{a^2d}{b^2+cd}$ respectively. Note that E_2 and E_3 lie inside the spheres S_a and S_b respectively, but outside the overlap region and the point E_4 lies inside the overlap region. The image singularities are located at these points (i.e., at E_2, E_3 and E_4). In contrast to the previous example, the image points are now shifted away from O, O' and D. It is

clear that the locations of the image points are dictated by the location of the initial stokeslet. Now the image system in the continuous phase consists of:

- stokeslet at E_2, E_3 and E_4,
- stokes-doublet at E_3 and E_4 and
- degenerate stokes-quadrupole at E_3 and E_4.

The strengths of the image singularities depend on the radii, the location of the initial stokeslet and the viscosity ratio. It is interesting to note that the image system for a stokeslet near a viscous drop also has the same type of singularities (with different strengths) as the hybrid drop. But the location of the image singularities in the former is at a single point, namely, the inverse point. The drag force on the hybrid droplet found in a similar manner as in the paraboloidal flow case is given by

$$\mathbf{F} = D_3\hat{e}_z\left\{\frac{a}{c+d} + \Lambda\left[\frac{b}{2d}\left(3-\frac{b^2}{d^2}\right) - \frac{ab}{2(b^2+cd)}\left(3-\frac{b^2(c+d)^2}{(b^2+cd)^2}\right)\right] + (1-\Lambda)\left[\frac{b}{d} - \frac{ab}{b^2+cd}\right]\right\}. \tag{29}$$

It can be seen from (29) that the drag force on the hybrid drop in a stokeslet flow depends on viscosity ratio, radii and the location of initial stokeslet. We discuss briefly the variation of drag force with these parameters. In Fig. 2(a) we have plotted

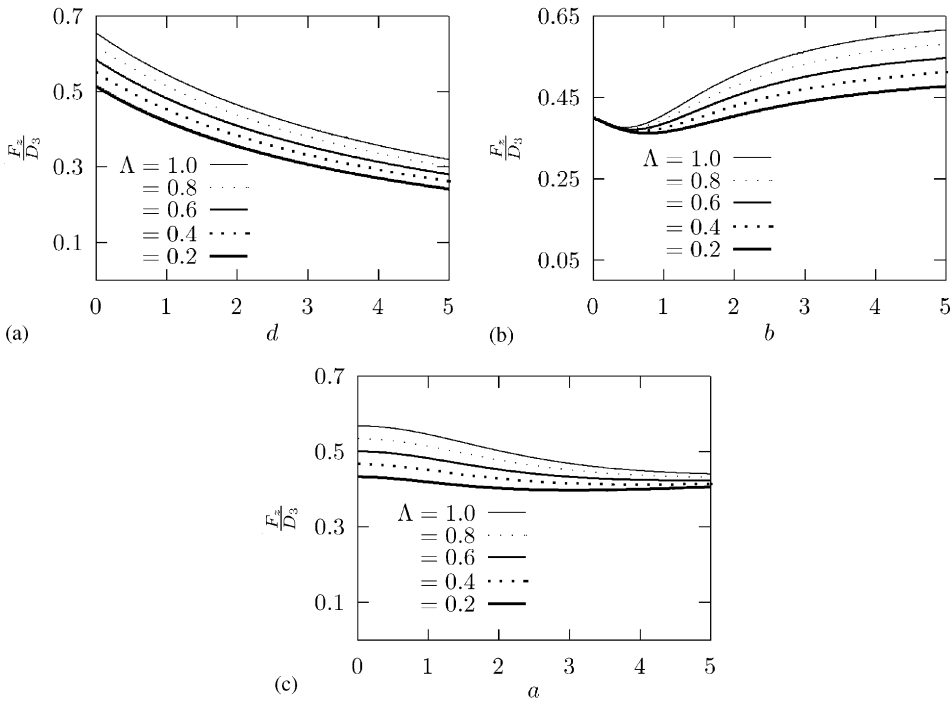

Fig. 2. Drag force in a single stokeslet flow: (a) $a = 1$, $b = 2$; (b) $a = 2$, $d = b + 1$; (c) $b = 2$, $d = 3$.

$\frac{F_z}{D_3}$ against the location of the stokeslet d for different viscosity ratios for $a = 1$ and $b = 2$. The drag decreases for increasing value of d as expected. This means that the droplet experiences greater resistance in stokeslet flow if the stokeslet is closer to it. Fig. 2(b) shows the variation of drag force against the radius 'b' when the stokeslet location is fixed at $d = 1$. In this case, the drag force decreases until $b \approx 0.5$ and then starts increasing with increasing values of b. This, in turn, implies that the resistance is greater when the liquid volume is large compared to the vapor volume. The variation of $\frac{F_z}{D_3}$ for different values of vapor radii are shown in Fig. 2(c). The curves for different viscosity ratios show that the drag decreases gradually until it becomes a constant in each case. It may be noticed that the drag force in general lies between the vapor–solid and vapor–vapor assembly limits. When $\Lambda = 1$, the expression (29) yields the force on a vapor–solid assembly while for $\Lambda = 0$, it reduces to the drag force on a vapor–vapor assembly (composite bubble).

After some calculation we find that expression for the capillary pressure T (see (7)) for the stokeslet flow, calculated from (7), is given by

$$T(\gamma_{II,III}) = \left[-p_{vapor} + \frac{\Lambda}{4\pi b^2}\left[\frac{\partial}{\partial r'}\left(G + r'\,\frac{\partial G}{\partial r'}\right) + \frac{2}{\rho'}\,\frac{\partial G_1}{\partial \theta'}\right]\right], \tag{30}$$

where

$$G = r'\left(\frac{b^2 - d_2^2}{d_2 r_2} - \frac{d^2 - b^2}{d r_1}\right), \quad G_1 = \rho'^2\left(\frac{d^2 - b^2}{r_1^3} - \frac{d_2^2 - b^2}{r_2^3}\right), \quad d_2 = \frac{b^2 + cd}{c + d}\,.$$

The stokeslet solution can be applied to the derivation of an approximate expression for the drag on a particle situated at $x = y = 0$, $z = c + d$, which translates without rotation parallel to the z-axis with velocity $V\hat{e}_z$. The axis of translation is assumed to be a principal axis of resistance of the particle. The $F\hat{e}_z$ and $F_\infty \hat{e}_z$ denote the viscous drag forces experienced by the particle with and without the presence of the hybrid droplet respectively. If a_1 denotes typical dimension and $h = d - c - b$ measures the distance of a suitable center E_1 of the translating body from the surface of the two-sphere assembly, then according to Brenner [26]

$$\frac{F}{F_\infty} = \frac{1}{1 - k_1(F_\infty/6\pi\mu^{(1)}Vh)} + O(\varepsilon^2)\,, \tag{31}$$

where $\varepsilon = a_1/h$ and the drag factor k_1 is defined by

$$k_1 = -\frac{3}{4} f(a, b, c, \Lambda)(\mathbf{q}^*(E_1) \cdot \hat{e}_z)\,, \tag{32}$$

$\mathbf{q}^*(E_1)$ being the regular part of the stokeslet velocity field at E_1, i.e., that arising from $\psi^{(1)^*} = \psi^{(1)} - \psi_0$, evaluated as the center $E_1(0, 0, c + d)$ of the body. In (32) $f(a, b, c, \Lambda)$ has a dimension of length and may be obtained from Eq. (26) of [11] as

$$f(a, b, c, \Lambda) = \left[2a + \Lambda\left(3b - \frac{ab}{c}\left(3 - \frac{b^2}{c^2}\right)\right) + (1 - \Lambda)\left(2b - \frac{2ab}{c}\right)\right]. \tag{33}$$

Using (10), (11) and (31) in (32), we find

$$k_1 = \frac{3}{2} f(a,b,c)\left\{ \frac{a}{(c+d)^2 - a^2} + \Lambda \left[\frac{3b}{2(d^2-b^2)} - \left(\frac{ab}{2(b^2+cd)} \left(3 - \frac{b^2}{d^2}\right) + \frac{ab^3(d^2-b^2)(d^2+b^2+cd)}{2d^2(b^2+cd)} \right) \frac{1}{\left(c+d-\frac{a^2 d}{b^2+cd}\right)} + \frac{a^5 b^3 (d^2-b^2)^2}{2(b^2+cd)^5} \frac{1}{\left(c+d-\frac{a^2 d}{b^2+cd}\right)^3} + \frac{a^3 b^3 (d^2-b^2)(c+d)}{(b^2-cd)^4} \frac{1}{\left(c+d-\frac{a^2 d}{b^2+cd}\right)^2} \right] + (1-\Lambda)\left[\frac{b}{d^2-b^2} - \frac{ab}{b^2+cd} \frac{1}{(c+d-\frac{a^2 d}{b^2+cd})} \right] \right\}. \tag{34}$$

The following limiting cases can be obtained from (34):

(i) When $a = 0$, Eq. (34) yields

$$k_1 = \frac{3}{2} b \left[\Lambda \frac{3b}{2(d^2-b^2)} + (1-\Lambda) \frac{b}{(d^2-b^2)} \right],$$

which is the drag factor for a spherical drop.

(ii) If we put $\Lambda = 1$, & $a = 0$ in (34), we obtain the drag factor for a solid sphere [23] given by

$$k_1 = \frac{9}{4} \frac{b^2}{(d^2-b^2)}.$$

(iii) In the limit $b \to d$, $a = 0$ and $\Lambda = 1$, (34) reduces to

$$k_1 = \frac{9}{8},$$

which is the drag factor for a plane wall [26]. Note that the cases (ii) and (iii) also follow from (i). Expression (34) gives the drag factor which can be used in (31) to calculate the approximate drag for a particle located near the hybrid droplet.

Expressions (26) and (27) correspond to a stokeslet located by the side of liquid spherical surface. The solution for a stokeslet situated on the vapor side may also be derived in the same way. For future reference we give here the stream functions due to a stokeslet located on the vapor side. For the fluid exterior to the droplet

we have (from (19))

$$\psi^{(1)}(\rho,z) = \frac{D_3}{8\pi\mu^{(1)}}\frac{\rho_1^2}{r_1} - \frac{D_3}{8\pi\mu^{(1)}}\frac{a}{d_a}\frac{\rho_2^2}{r_2} + \frac{D_3}{8\pi\mu^{(1)}}\Lambda\left[-\frac{b}{2(c+d_a)}\left(3-\frac{b^2}{(c+d_a)^2}\right)\frac{\rho_3^2}{r_3} + \frac{b^3((c+d_a)^2-b^2)^2}{2(c+d_a)^5}\frac{\rho_3^2}{r_3^3} - \frac{b^3((c+d_a)^2-b^2)}{(c+d_a)^4}\frac{\rho_3^2 z_3}{r_3^3}\right] - \frac{D_3}{8\pi\mu^{(1)}}(1-\Lambda)\frac{b}{(c+d_a)}\frac{\rho_3^2}{r_3} + \frac{D_3}{8\pi\mu^{(1)}}\Lambda\left\{\left[\frac{ab}{2(a^2+cd_a)}\left(3-\frac{b^2d_a^2}{(a^2+cd_a)^2}\right)\right]\frac{\rho_4^2}{r_4} - \frac{a^3b^3((c+d_a)^2-b^2)d_a}{(a^2+cd_a)^4}\frac{\rho_4^2 z_4}{r_4^3} - \frac{a^5b^3((c+d_a)^2-b^2)^2}{2(a^2+cd_a)^5}\frac{\rho_4^2}{r_4^3}\right\} + \frac{D_3}{8\pi\mu^{(1)}}(1-\Lambda)\frac{ab}{a^2+cd_a}\frac{\rho_4^2}{r_4}\,, \tag{35}$$

and for the fluid inside the droplet (from (20))

$$\psi^{(2)}(\rho,z) = (1-\Lambda)\frac{(r'^2-b^2)}{2b^2}\frac{D_3}{8\pi\mu^{(1)}}\left[-3+2r'\frac{\partial}{\partial r'} - \frac{(r'^2-b^2)}{2}L_{-1}\right]\left(\frac{\rho_1^2}{r_1} - \frac{a}{d_a}\frac{\rho_2^2}{r_2}\right). \tag{36}$$

The notation is the same as those for the stokeslet on the liquid spherical side with appropriate modifications. For example, r_j in the present case is given by

$$r_j^2 = r^2 + 2OO_j r\cos\theta + OO_j^2 \quad (j=1,2,3,4)\,. \tag{37}$$

The distances OO_j are now $OO_1 = d_a$, $OO_2 = \frac{a^2}{d_a}$, $OO_3 = \frac{a^2+cd_a}{c+d_a}$, $OO_4 = \frac{a^2(c+d_a)}{a^2+cd_a}$ respectively. The quantities such as drag and approximate expression for drag on a particle situated near the droplet may also be computed in this case. For brevity, we shall not repeat those calculations and discussions here. However, expressions (35) and (36) will be used in a later section to show the streamline patterns in a variety of circumstances.

5.3. Point-source doublet outside Γ

Finally, we consider a degenerate Stokes-quadrupole (potential-doublet) of strength $\frac{D_3}{6\pi\mu^{(1)}}$ located at E_1. The stream function corresponding to this singularity in an unbounded fluid is

$$\psi_0(\rho,z) = \frac{D_3}{6\pi\mu^{(1)}}\frac{\rho_1^2}{r_1^3}\,.$$

The perturbed stream functions in the presence of the hybrid droplet is

$$\begin{aligned}\psi^{(1)}(\rho,z) = {} & \frac{D_3}{6\pi\mu^{(1)}}\frac{\rho_1^2}{r_1^3} - \frac{D_3}{6\pi\mu^{(1)}}\left[\frac{a}{(c+d)^3}\frac{\rho_2^2}{r_2} + 2\,\frac{a^3}{(c+d)^4}\frac{\rho_2^2 z_2}{r_2^3} + \frac{a^5}{(c+d)^5}\frac{\rho_2^2}{r_2^3}\right] \\ & + \frac{D_3}{6\pi\mu^{(1)}}\Lambda\left[\frac{b^3}{2d^3 r_3^3}\left(1-\frac{3b^2}{d^2}\right) - \frac{3b}{2d^3 r_3} - \frac{6b^3}{d^4}\frac{z_3}{r_3^3}\right. \\ & \left. - \frac{3b^5(b^2-d^2)}{d^6}\frac{z_3}{r_3^5} - \frac{6b^5}{d^5}\frac{z_3^2}{r_3^5}\right]\rho_3^2 \\ & - \frac{D_3}{6\pi\mu^{(1)}}(1-\Lambda)\left[\frac{b}{d^3}\frac{\rho_3^2}{r_3} - 2\,\frac{b^3}{d^4}\frac{\rho_3^2 z_3}{r_3^3} + \frac{b^5}{d^5}\frac{\rho_3^2}{r_3^3}\right] \\ & + \frac{D_3}{6\pi\mu^{(1)}}\Lambda\left\{\frac{3ab}{2d^2(b^2+cd)^3}\left(a^2d^2 - b^2(b^2+cd)\right.\right. \\ & \left.\left. + \frac{b^4(d^2+b^2+2cd)}{b^2+cd}\right)\frac{\rho_4^2}{r_4}\right. \\ & + \frac{a^5b^3}{2(b^2+cd)^6}((d^2-b^2)(b^2-cd) + 2b^2(b^2+cd))\frac{\rho_4^2}{r_4^3} \\ & - \frac{a^3b^3}{d(b^2+cd)^5}(2b^2(3b^2+5d^2) + cd(d^2+15b^2+6cd))\frac{\rho_4^2 z_4}{r_4^3} \\ & \left. + \frac{6a^5b^5(c+d)d}{(b^2+cd)^6}\frac{\rho_4^2 z_4^2}{r_4^5} + \frac{3a^7b^5d(d^2-b^2)}{(b^2+cd)^7}\frac{\rho_4^2 z_4}{r_4^4}\right\} \\ & + \frac{D_3}{6\pi\mu^{(1)}}(1-\Lambda)\left[\frac{abc^2}{(b^2+cd)^3}\frac{\rho_4^2}{r_4} - \frac{2a^3b^3c}{(b^2+cd)^4}\frac{\rho_4^2 z_4}{r_4^3}\right. \\ & \left. + \frac{a^5b^5}{(b^2+cd)^5}\frac{\rho_4^2}{r_4^3}\right], \end{aligned} \tag{38}$$

for the continuous phase and

$$\begin{aligned}\psi^{(2)}(\rho,z) = {} & (1-\Lambda)\frac{(r'^2-b^2)}{2b^2}\frac{D_3}{6\pi\mu^{(1)}}\left[-3 + 2r'\frac{\partial}{\partial r'} - \frac{(r'^2-b^2)}{2}L_{-1}\right] \\ & \left\{\frac{\rho_1^2}{r_1^3} - \left(\frac{a}{(c+d)^3}\frac{\rho_2^2}{r_2} + 2\,\frac{a^3}{(c+d)^4}\frac{\rho_2^2 z_2}{r_2^3} + \frac{a^5}{(c+d)^5}\frac{\rho_2^2}{r_2^3}\right)\right\}, \end{aligned} \tag{39}$$

for the dispersed phase. The image system in the continuous phase consists of the following:

- Stokeslet at E_2, E_3, E_4
- Stokes-doublet at E_2, E_3, E_4
- Degenerate Stokes-quadrupole at E_2, E_3, E_4
- Non-degenerate Stokes-quadrupole at E_3, E_4
- Degenerate Stokes-octupole (potential-quadrupole) at E_3, E_4.

Here, the notation ($E_1, E_2, \ldots$ etc.) is the same as those defined in the stokeslet case. Here also, the strengths of image singularities depend on the radii of the two spheres, the viscosity ratio and the location of the initial singularity. As in the preceding example, the image points are controlled by the location of the initial singularity. The type of image singularities in the present case are also the same as in the case of viscous drop [25]. The drag force on the hybrid droplet is found to be

$$\mathbf{F} = D_3\hat{e}_z\left\{\frac{a}{(c+d)^3} + \Lambda\left[\frac{3b}{2d^3} - \frac{3ab}{d^2(b^2+cd)^3}\left(a^2d^2 - b^2(b^2+cd) + \frac{b^4(d^2+b^2+2cd)}{b^2+cd}\right)\right] + (1-\Lambda)\left[\frac{b}{d^3} - \frac{abc^2}{(b^2+cd)^3}\right]\right\}. \tag{40}$$

The drag force $\frac{F_z}{D_3}$ has been plotted against the following parameters: location of the singularity (d), and the radii (a, b) for several viscosity ratios Λ in Fig. 3. As in the single stokeslet case, the drag decreases as the dipole moves away from the droplet (see Fig. 3(a)). The behavior of the drag force against the radius b is somewhat different (Fig. 3(b)) when the dipole is at a fixed distance from the droplet surface. At first, it starts decreasing up to $b \approx 0.5$, thereafter it increases until $b \approx 1.2$ where it attains its maximum value, and then decreases gradually with increasing values of b. It follows that the drag in dipole induced flow is maximum when the vapor radius a

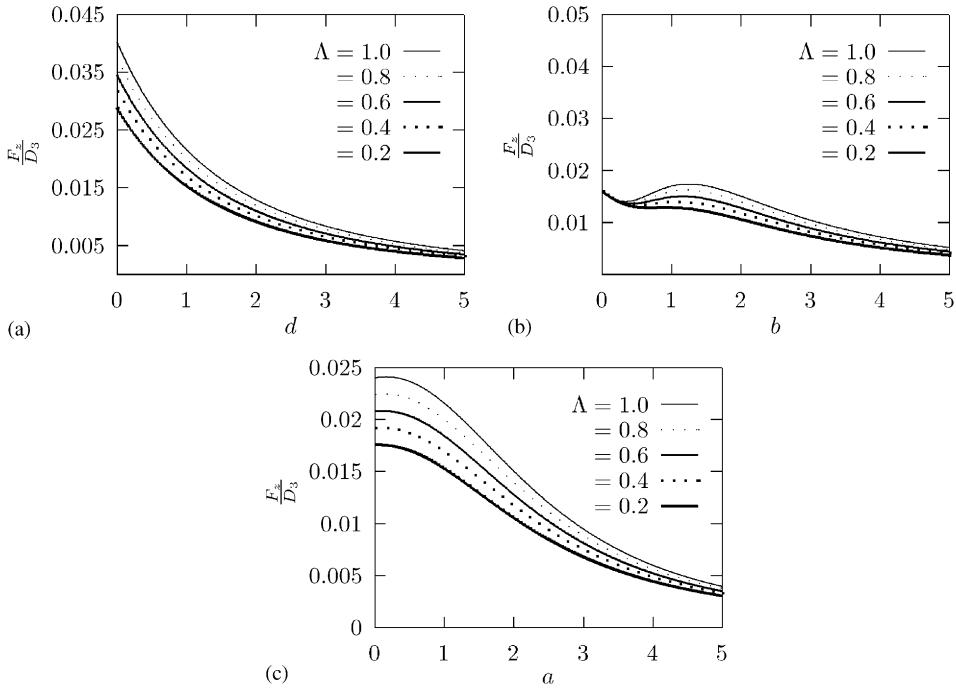

Fig. 3. Drag force in a potential-dipole flow: (a) $a = 1$, $b = 2$; (b) $a = 2$, $d = b + 1$; (c) $b = 2$, $d = 3$.

is $\frac{5}{3}$ times larger than the liquid spherical radius b. Fig. 3(c) shows that the increase of vapor radius also reduces the drag force. For the extremal values of Λ, (40) reduces to that of vapor–solid and vapor–vapor assembly limits respectively.

An explanation for the hump in Fig. 3(b) is warranted here. For extreme values of b (small and large), the hybrid geometry is mostly a sphere, either a bubble (small b) or a droplet (large b). Drag for a single sphere due to a dipole located at $b+1$ is known to be proportional to $\frac{b}{b+1}$. In fact, it follows from Eq. (40) that this drag for a single vapor bubble is $\frac{b}{b+1}$ and that for a single spherical droplet is $\frac{3}{2}\frac{b}{b+1}$. This explains as to why the drag in this figure decreases with increasing b (radius of the spherical surface of the droplet) for extreme values of b. For intermediate values of b, both the vapor and the droplet surfaces become relatively comparable and the drag results due to contribution from both which is bound to be more than the drag for either of the single sphere case which explains the hump in this figure.

After some calculation we find that expression for the capillary pressure T (see (7)) for the present case, calculated using (7), is given by

$$T(\gamma_{II,III}) = \left[-p_{vapor} + \frac{\Lambda}{4\pi b^2}\left[\frac{\partial}{\partial r'}\left(G + r'\frac{\partial G}{\partial r'}\right) + \frac{2}{\rho'}\frac{\partial G_1}{\partial \theta'}\right]\right]_{r'=b}, \tag{41}$$

where

$$G = r'\left\{\frac{3}{dr_1} + \frac{2z_1}{r_1^3} + \frac{a}{(c+d)^3}\left[\frac{(b^2-d_2^2)}{d_2 r_2} + \frac{2a^2}{c+d}\left((b^2-d_2^2)\left(\frac{1}{d_2^2 r_2} + \frac{z_2}{d_2 r_2^3}\right) - \frac{2}{r_2}\right) + \frac{a^4}{(c+d)^2}\left(\frac{3}{d_2 r_2} - \frac{2z_2}{r_2^3}\right)\right]\right\},$$

$$G_1 = \rho'^2\left\{-\frac{5}{r_1^3} - \frac{6dz_1}{r_1^5} + \frac{a}{(c+d)^3}\left[\frac{(b^2-d_2^2)}{r_2^3} + \frac{2a^2}{c+d}\left((b^2-d_2^2)\frac{3z_2}{r_2^5} - \frac{2d_2}{r_2^3}\right) + \frac{a^4}{(c+d)^2}\left(\frac{5}{r_2^3} - \frac{6d_2 z_2}{r_2^5}\right)\right]\right\}.$$

6. Drag on the hybrid droplet: an observation

As shown through three axisymmetric flows in the previous section, expressions (19) and (20) are sufficient for the purpose of obtaining the flow fields in the two phases and calculating the drag acting on the droplet. The formula for the drag in each of these cases can also be obtained from a more general expression for the drag force which we provide below. For this purpose, we need to state the unbounded flow fields with regard to S_a and S_b. From (19), we see that the first and second terms correspond to the unbounded flow fields for the sphere S_b, which we denote by $\mathbf{q}_0, p_0$ and $\mathbf{q}_{0a}, p_{0a}$. Likewise, the first and last two terms of (19) correspond to unbounded flow fields for the sphere S_a, denoted by $\mathbf{q}_0$, p_0 and $\mathbf{q}_{0b}$, p_{0b}. We conjecture the

following general expression for the drag force $\mathbf{F}$ on the hybrid droplet in arbitrary axisymmetric flows from the results on drag in three cases obtained in the previous section and the known Faxen relations for the spherical bubble and spherical drop [15,16].

$$\mathbf{F} = 4\pi\mu^{(1)}\left\{[a\mathbf{q}_0]_O + (1-\Lambda)\left([b\mathbf{q}_0]_{O'} - \left[\frac{ab}{c}\,\mathbf{q}_0\right]_D\right)\right\} + 6\pi\mu^{(1)}b\Lambda\left\{[(\mathbf{q}_0+\mathbf{q}_{0a})]_{O'} + \frac{b^2}{6}[\nabla^2(\mathbf{q}_0+\mathbf{q}_{0a})]_{O'}\right\}, \tag{42}$$

where

$$\mathbf{q}_{0a} = -\mathrm{curl}\left(\hat{e}_\phi\,\frac{r^3}{a^3}\,\psi_0\left(\frac{a^2}{r^2}\,\rho, \frac{a^2}{r^2}\,z\right)\right), \tag{43}$$

$\hat{e}_\phi$ being the unit vector in azimuthal direction. The subscripts outside the square brackets in (42) indicate evaluation of quantities at those points.

In the literature, a variety of Faxen laws for calculating various multipole moments such as force, torque, stresslet coefficients, etc. has been derived for several particle shapes (sphere, spheroid, ellipsoid) and several physical problems [27–32]. The above conjecture (42) for the drag force may be considered a Faxen-type relation for the hybrid droplet in axisymmetric flow. It may be worthwhile to prove this conjecture (42) in a rigorous way. One can verify that formulas for the drag in each of the three cases obtained in the previous section follows from (42). We can also see that if we set $a = 0$ in (42), we recover the Faxen law for a single stress-free sphere [15,16]. The Faxen law for a fluid sphere may be deduced from (42) by setting $b = 0$ [15,16]. In the latter case, the quantity $\mathbf{q}_{0a}$ is irrelevant.

Now we discuss the force that the interior interface may experience, if any. As far as the vapor–solid (i.e., $\mu^{(2)} \to \infty$) and vapor–vapor (i.e., $\mu^{(2)} \to 0$) assemblies are concerned, the issue that the full boundary conditions are not satisfied at the interior interface AB (see Fig. 1) does not arise. However, in the vapor–liquid case, the stresses on the interface may influence the net force. In this case, if desired the stresses on the interior interface AB may be computed using $2\pi b^2 \int_{AB}[-\tau^{(2)}_{r'r'}\cos\theta' + \tau^{(2)}_{r'\theta'}\sin\theta']_{r'=b}\sin\theta'\,\mathrm{d}\theta'$. The stress components $\tau^{(2)}_{r'r'}$ is given before just after Eq. (7) and $\tau^{(2)}_{r'\theta'} = \mu^{(2)}\left(\frac{\partial q^2_{r'}}{\partial\theta'} + r'\,\frac{\partial}{\partial r'}\left(\frac{q^{(2)}_{\theta'}}{r'}\right)\right)$,where the $q_{r'}$ and $q_{\theta'}$ in terms of stream function are already given in (10) and (11) respectively.

7. Streamline patterns

The solutions obtained in the previous section can be used to discuss the flow patterns in each case. The flow streamlines have been plotted under a variety of circumstances in each case. In many instances, they show rather interesting flow patterns. We describe the flow behavior in each case separately. It may be noted that

in the figures below the two spherical segments have been extended inside the hybrid drop with dotted lines. However, the interface separating the dispersed phase and the vapor not the interface because the actual interface is the dotted segment $r' = b$ (extended part of the larger sphere inside the hybrid droplet—also see Fig. 1).

7.1. Paraboloidal flow

Fig. 4 shows the streamline patterns for paraboloidal flow, for several viscosity ratios Λ. The plots are sketched using expressions (21) and (22). We find that when $b/a = 2$, the streamlines in the continuous phase are slightly curved in the neighborhood of the larger spherical surface Γ_b and straight everywhere else for $\Lambda < 0.853$ (approximately). When Λ takes this value, an eddy of infinitesimal small size appears in front of the large sphere. It appears as a spot in Fig. 4(b). The size of this eddy grows monotonically with the viscosity ratio Λ as shown in Fig. 4(c) and (d). For $\Lambda = 1$, i.e., for the vapor–solid assembly, the eddy has maximum size which is shown in Fig. 4(d). It is interesting that there is no eddy on the vapor side for any value of Λ. Perhaps the presence of the vapor prevents the formation of eddy for these parameter values.

However, if $b/a = 3$, a pair of eddies appears on either side of the droplet as demonstrated in Fig. 5. In this case, a single eddy appears for $\Lambda \approx 0.3818$ near the larger spherical surface. Further increase of the viscosity ratio generates another eddy on the vapor side and also increases the size of the one that already exists. The sizes of these pair of eddies grow as we increase the value of the viscosity ratio. At $\Lambda = 1$, these eddies become large and equal, and come very close to the droplet. Therefore, it is clear that the viscosity ratio and the radii dictate the existence/non-existence of single or a pair of eddies in the paraboloidal flows. The flow streamlines in the dispersed phase do not change significantly with these parameters.

We provide some (speculative) explanation for the eddies in Fig. 4. In low Reynolds number flow past an object with no-slip boundary condition, eddies

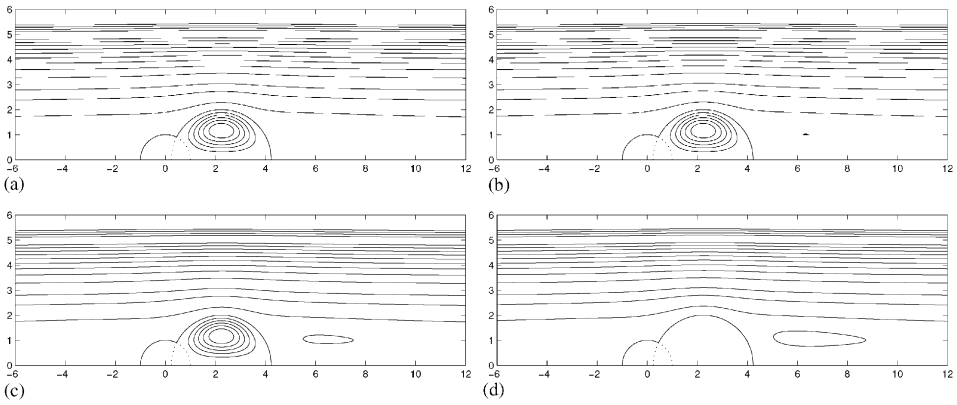

Fig. 4. Streamlines in paraboloidal flow with $a = 1$, $b = 2$ for various values of Λ: (a) $\Lambda = 0.8$; (b) 0.853; (c) 0.9; (d) 1.0.

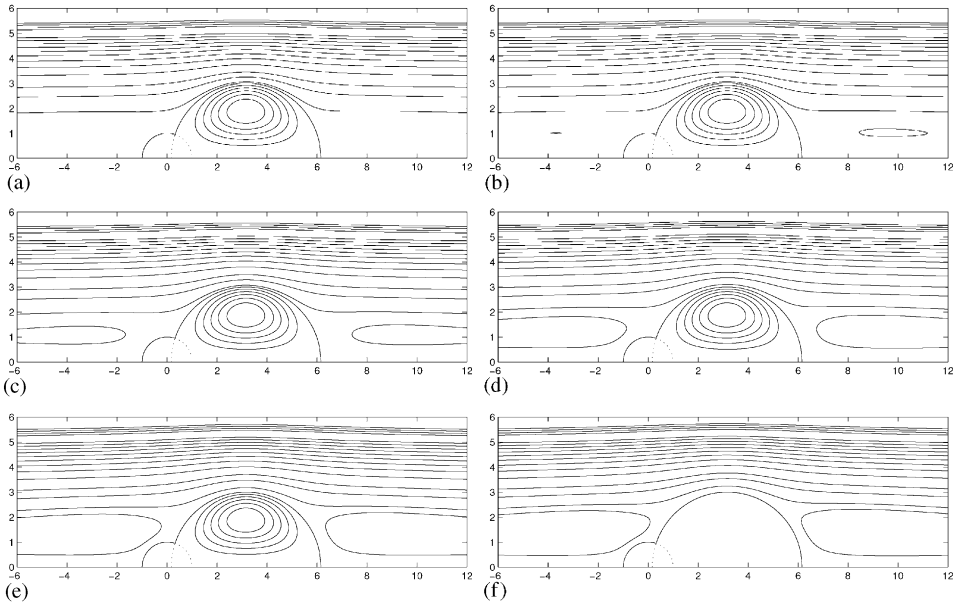

Fig. 5. Flow streamlines in paraboloidal flow with $a = 1$, $b = 3$ for various values of Λ: (a) $\Lambda = 0.3818$; (b) 0.4005; (c) 0.5; (d) 0.7; (e) 0.9; (f) 1.0.

usually appear behind the object (downstream) due to separation effect. Some such interesting flows can be found in Van Dyke [33]. On the other hand, in inviscid flows no such eddies appear due to pure-slip on the boundary of the object. Our study here for viscous flow covers these two limiting cases: from no-slip ($\Lambda = 1$) to pure-slip ($\Lambda = 0$) respectively as far as the larger spherical surface is concerned. With increasing values of viscosity inside the larger sphere (which is equivalent to increasing values of Λ) in Fig. 4(a) through 4(d), the fluid velocity on the larger spherical surface gradually decreases, as expected, until it becomes zero on this surface in Fig. 4(d) ($\Lambda = 1$) where the geometry corresponds to a vapor–solid assembly. Therefore, it is expected that as Λ increases, eddies should first appear at some value of Λ. Fig. 4(b) shows that this happens for a value $\Lambda \approx 0.853$ where the larger spherical surface is close to being that of a solid boundary, in the sense that the fluid on the larger spherical surface is almost close to being stagnant (no-slip condition). Further increase in Λ causes the fluid velocity on the larger spherical surface to decrease even further resulting in an increase in the size of the eddy. Eventually the eddy in Fig. 4(d) ($\Lambda = 1$) assumes the maximum size due to separation of the fluid from the solid sphere (larger).

Explanation for eddies behind the larger spherical surface in Fig. 5(a)–(f) is similar except that the eddies first appear at a smaller value of Λ ($\Lambda \approx 0.3818$) which is expected because the radius of the larger spherical surface here is greater than the same in Fig. 4. Here eddies also appear behind the vapor side of the hybrid droplet. Perhaps this is easier to explain once we accept, quite correctly based on the above

explanation, that eddies identical to the one in front of the larger spherical surface should appear in the limit of vanishing size of the smaller spherical surface. Then the effect of the finite size of the smaller spherical surface is to delay the appearance of the eddies behind this surface. Therefore, the size of the eddies behind the vapor side is smaller than the ones on the droplet side in Fig. 5(b) through 5(f). It may happen that for large enough size of the smaller spherical surface compared to the larger spherical surface, the onset phenomena of the appearance of the eddies may be completely suppressed as, perhaps, is the case in Fig. 4.

7.2. Stokeslet

As stated earlier, one could consider many situations involving a single or a pair of stokeslets in the presence of a hybrid droplet. Expressions (26)–(27) and (35) and (36) are sufficient to sketch the streamlines in different cases. In the following we discuss the flow patterns in each case separately.

7.2.1. Single stokeslet

We first consider a single stokeslet with positive strength located in front of S_b first, and then in front of S_a on the axis of symmetry. In both situations, the flow streamlines in the continuous phase are as expected. The presence of the hybrid droplet has no effect in stokeslet flow as can be seen from Fig. 6(a) and (b). The eddy in the dispersed phase moves towards the stokeslet in both the Figures. The other parameters such as viscosity ratio, radii and location of initial stokeslet do not seem to affect the flow patterns.

7.2.2. Two identical stokeslets

In the following, we use the terminology "two identical stokeslets" to refer to two stokeslets with the same positive strength. We now consider the situation when two identical stokeslets are situated on each side of the droplet. When the two stokeslets are located at equi-distance from each spherical surface (i.e., $d = b + 1, d_a = a + 1$), the blending of streamlines emanating from each stokeslet is smooth as evident from Fig. 6(c). As the stokeslets get closer to the droplet with the equidistant constraint, then the fluid velocity is more near the stokeslet on the vapor side (Fig. 6(d)). If we fix the location of one stokeslet and move the other closer to the droplet, then the fluid velocity is more near the one that is farthest from the droplet (Fig. 6(e) and (f)). The streamlines in the dispersed phase form a single eddy structure as in the case of single stokeslet. The core of this single eddy appears to be tilted towards the vapor. From this analysis we may conclude that eddies do not appear in the continuous phase.

7.2.3. Two opposite stokeslets

Next we consider the case when the droplet is placed between two opposite stokeslets. In the following, we use the terminology "two opposite stokeslets" to refer to two stokeslets: one with the positive strength, and the other with equal but negative strength. We choose the one which is on the vapor side to have positive strength and the other on the liquid side to have an equal but negative strength.

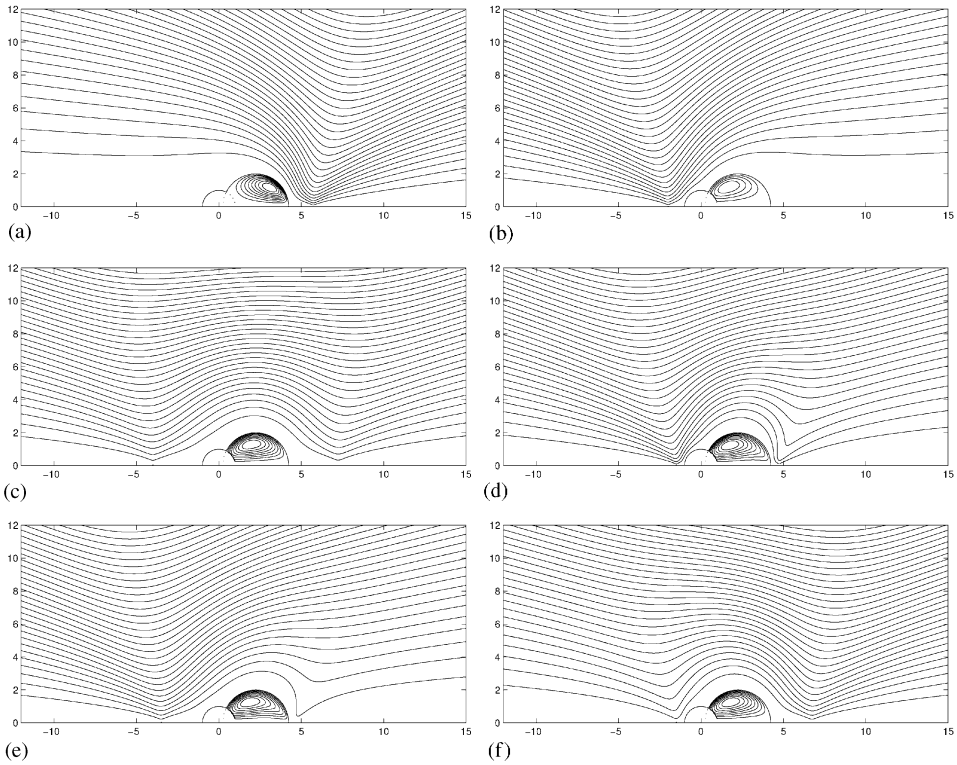

Fig. 6. Streamline plots in stokeslet flow with $a = 1$, $b = 2$, $\Lambda = 0.5$ for various locations: (a) single stokeslet near S_b with $d = b + 1.5$; (b) single stokeslet near S_a with $d_a = a + 1$; (c)–(f) pair of equal stokelets: (c) $d = b + 5.0$, $d_a = a + 5.0$; (d) $d = b + 0.5$, $d_a = a + 0.5$; (e) $d = b + 0.5$, $d_a = a + 0.25$; (f) $d = b + 0.25$, $d_a = a + 0.5$.

Here, the streamlines show fascinating flow patterns (see Fig. 7(a)–(f)). We demonstrate the stokeslet interactions in the presence of a hybrid droplet with respect to various parameters separately.

Fig. 7(a)–(f) shows the streamline patterns for the case of two opposite stokeslets for various locations. The locations of these two singularities are varied in such a way that they are situated at equi-distance from vapor and liquid spherical surfaces respectively. As said before, if the two stokeslets are far from the droplet, the interaction of the stokeslets is not stronger in the neighborhood of the droplet (see Fig. 7(a) and (b)). When they are moved closer, a single toroidal eddy structure appears in front of the liquid sphere. This moves the eddy further close to the droplet as the stokelets are moved nearer to the hybrid drop. We notice that the size and shape of these closed streamlines also change due to the stokeslets moving closer to the droplet. In the dispersed phase, two unequal eddy patterns appear. The larger eddy is closer to vapor bubbles. When the stokeslets are moved much closer to the droplet, the larger eddy increases in size and the smaller eddy becomes smaller. This is perhaps due to the geometrical asymmetry.

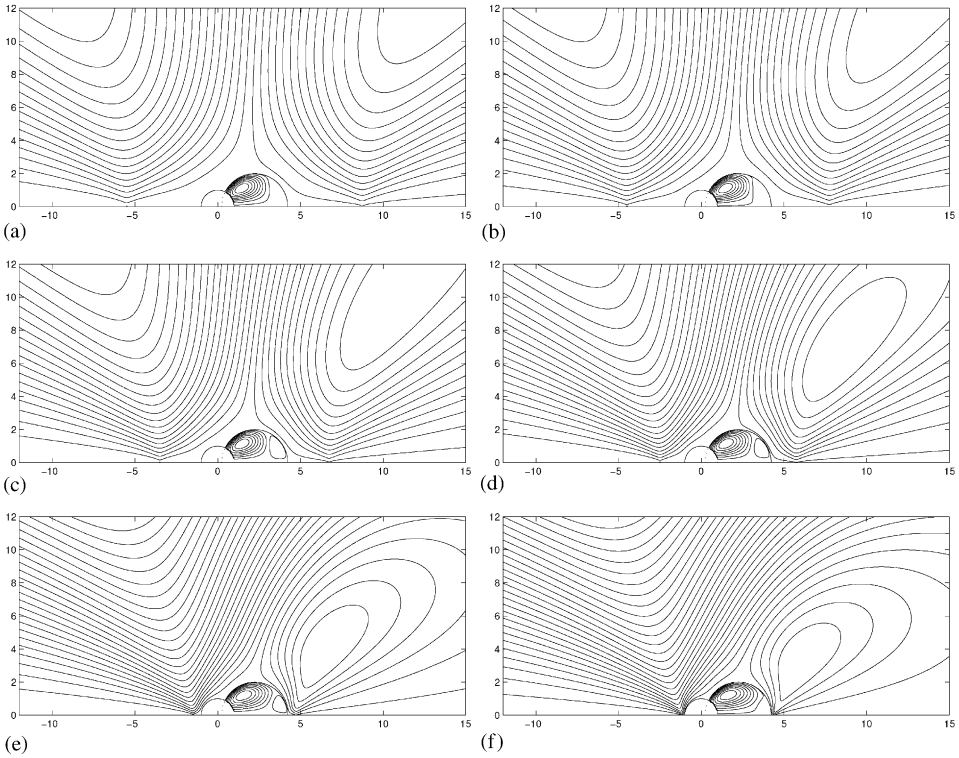

Fig. 7. Streamlines for a pair of opposite stokeslets with $a = 1$, $b = 2$, $\Lambda = 0.6$: (a) $d = b + 4.5$, $d_a = a + 4.5$; (b) $d = b + 3.5$, $d_a = a + 3.5$; (c) $d = b + 2.5$, $d_a = a + 2.5$; (d) $d = b + 1.5$, $d_a = a + 1.5$; (e) $d = b + 0.5$, $d_a = a + 0.5$; (f) $d = b + 0.2$, $d_a = a + 0.2$.

It is worthwhile to point out that the toroidal eddy discussed in the preceding paragraph has been found in different contexts. For a stokeslet oriented normal to a rigid plane boundary, a single toroidal eddy was discovered by Aderogba and Blake [34] (see also Refs. [35,36]). In an analogous problem in two dimensions, Blake and Otto [37] found a pair of toroidal eddies near the boundary. These authors used their closed streamline model to explain chaotic filtration through the concept of a *blinking stokeslet*, a stokeslet alternating its vertical position according to a specific protocol. The eddy structure reported here resembles those discussed in previous works ([34–36]). Similar eddies as reported in this paper have also been found in problems associated with a pulsating source [38]. We believe that the present results may be used in similar models but we are not concerned about those aspects here.

Next, we fix the location of one stokeslet and move the other towards the droplet relaxing the equidistance constraint. Fig. 8(a)–(f) shows the situation when the stokeslet on the vapor side is located at a fixed distance $d_a = 5.0$ and the other stokeslet is moved towards the droplet. The flow streamlines in the continuous phase reveals the existence of eddy structure. As in the previous situation, the single

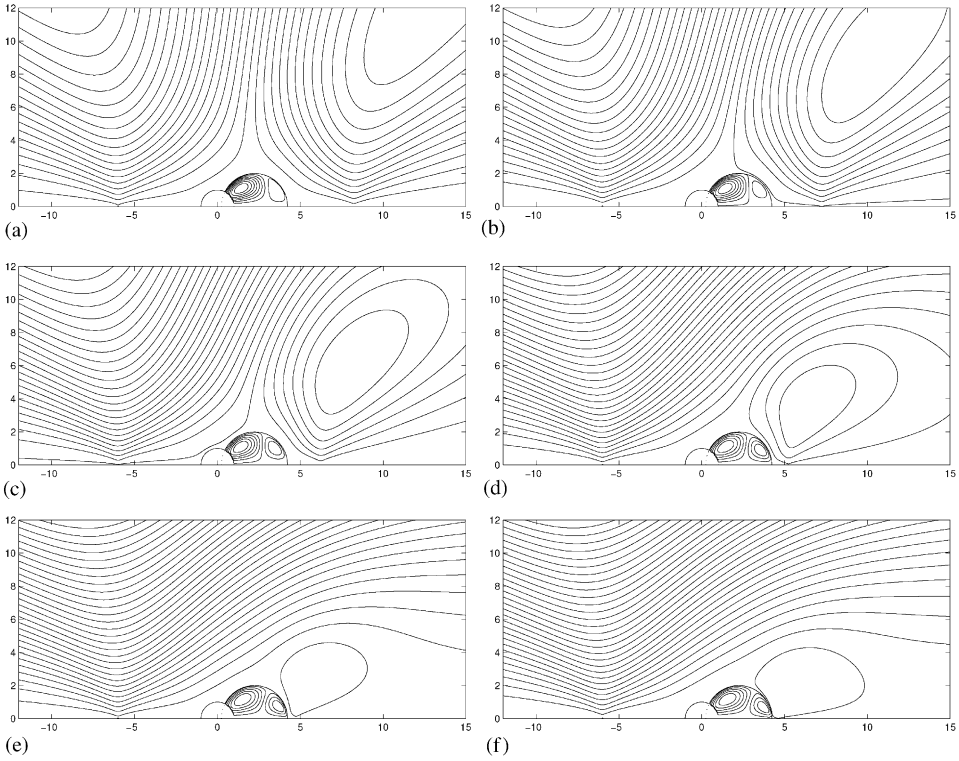

Fig. 8. Streamlines for a pair of opposite stokeslets with $a = 1$, $b = 2$, $\Lambda = 0.6$. Moving the stokeslet located in front of S_b. (a) $d = b + 4$, $d_a = a + 5$; (b) $d = b + 3$, $d_a = a + 5$; (c) $d = b + 2$, $d_a = a + 5$; (d) $d = b + 1$, $d_a = a + 5$; (e) $d = b + 0.5$, $d_a = a + 5$; (f) $d = b + 0.3$, $d_a = a + 5$.

toroidal eddy structure appears near the dispersed liquid phase. If the stokeslet moves closer to the droplet, this eddy also moves closer to the stokeslet. However, the flow streamlines in the dispersed phase exhibit a different behavior compared to the previous situation. The two unequal eddies exist even if the stokeslet is moved much closer to the droplet. This may be due to the fact that the fixed stokeslet being far from the droplet is unable to influence the flow in the dispersed phase.

Fig. 9(a)–(f) shows the case of moving the stokeslet on the vapor side keeping the other fixed. As we can see, the eddy structure now develops on the vapor side. It moves closer the droplet if the stokeslet is also brought closer to it. This is because the stokeslet on the liquid spherical surface side is far from the droplet. We notice that only one eddy appears in the dispersed phase unlike the previous situation. This is probably due to the fact that the stokeslet on the liquid spherical surface side is far from the droplet. Thus, the stokeslet locations in the case of two opposite stokeslets control the eddy structure in various situations.

We now discuss the effect of viscosity ratio on the flow patterns due to two opposite stokeslets. In Fig. 10(a)–(f) we have plotted the streamline patterns for

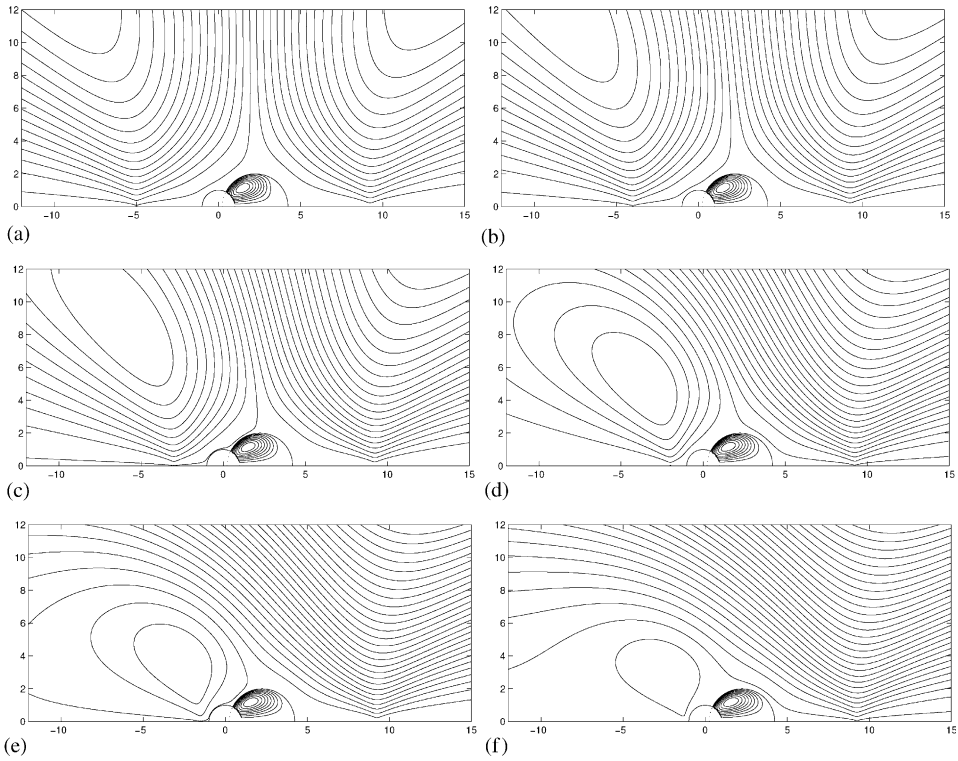

Fig. 9. Streamlines for a pair of opposite stokeslets with $a = 1$, $b = 2$, $\Lambda = 0.6$. Moving the stokeslet on the vapor side (a) $d = b + 5$, $d_a = a + 4$; (b) $d = b + 5$, $d_a = a + 3$; (c) $d = b + 5$, $d_a = a + 2$; (d) $d = b + 5$, $d_a = a + 1$; (e) $d = b + 5$, $d_a = a + 0.5$; (f) $d = b + 5$, $d_a = a + 0.3$.

several viscosity ratios in two cases: (i) when the two stokeslets are equi-distant from the droplet; and (ii) when they are not equi-distant. In the equi-distance case, the increase of viscosity ratio mildly rotates the eddy structure towards the axis of symmetry without changing its location with respect to the droplet. On the other hand, in the non-equi-distance case the eddy mildly turns away from the axis of symmetry (on the vapor side) with increasing values of viscosity ratio. All these features may be noticed in Fig. 10. In the dispersed phase, the pattern of the streamlines is identical to that of the previous situations.

7.3. Potential-dipole

The streamline patterns for the flow due to a potential-dipole in the presence of a hybrid droplet is shown in Fig. 11. It can be seen that the flow is smooth everywhere in the continuous phase for different values of the parameters. The eddy in the dispersed phase moves towards the dipole as the singularity moves towards the hybrid droplet. It may be worth studying such flows in the presence of a pair of

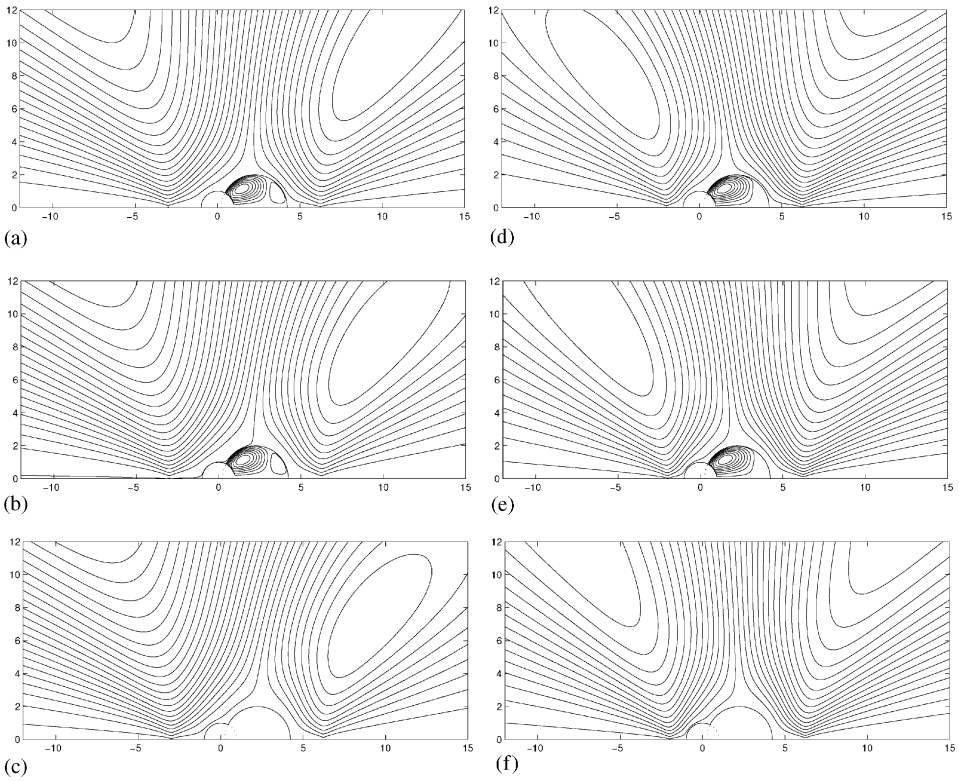

Fig. 10. Streamline patterns for a pair of opposite stokeslets with $a = 1$, $b = 2$ for various values of Λ and locations: (a) $d = b + 3$, $d_a = a + 3$, $\Lambda = 0.2$; (b) $d = b + 3$, $d_a = a + 3$, $\Lambda = 0.6$; (c) $d = b + 3$, $d_a = a + 3$, $\Lambda = 1.0$; (d) $d = b + 3$, $d_a = a + 2$, $\Lambda = 0.2$; (e) $d = b + 3$, $d_a = a + 1.0$, $\Lambda = 0.6$; (f) $d = b + 3$, $d_a = a + 1$, $\Lambda = 1.0$.

potential-dipoles using similar approaches. We do not feel it is necessary to pursue this study here.

8. Conclusion

We have presented simple formulas for calculating Stokes flow fields around a vapor–solid/vapor–vapor/vapor–liquid hybrid droplet suspended in general axisymmetric flows provided that the two spherical surfaces intersect orthogonally. Using these analytic formulas, we have found singularity solutions for a variety of primary flows including paraboloidal flow, flows due to a single and a pair of stokeslets, and a potential dipole. The exact solutions have been used to sketch the streamline patterns for a hybrid droplet. The streamline plots for paraboloidal flow and flow due to a pair of opposite stokeslets display eddy pattern. The existence, shape, size and location of this eddy structure depend on the viscosity ratio, the radii associated with

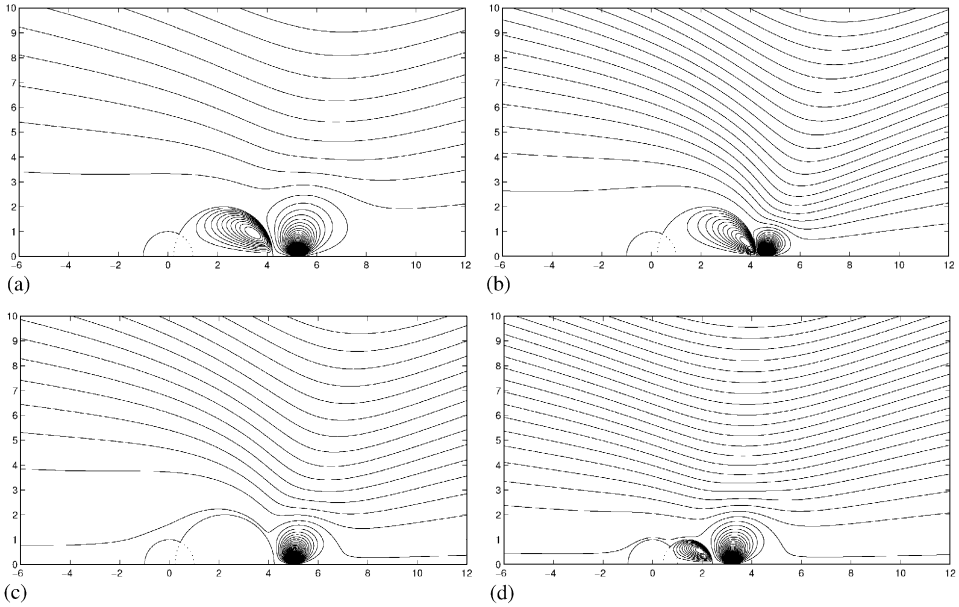

Fig. 11. Typical streamline patterns for flow around a vapor–liquid hybrid droplet due to a potential-dipole with $a = 1$, $b = 2$: (a) $d = b + 1$, $\Lambda = 0.5$; (b) $d = b + 0.4$, $\Lambda = 0.5$; (c) $d = b + 0.8$, $\Lambda = 1.0$; (d) $d = b + 0.8$, $\Lambda = 0.6$.

the geometry of the hybrid droplet, and the location of the stokeslets (in the case of singularity driven flow). The solutions for other complicated axisymmetric flows in the presence of a hybrid droplet can be found in a similar fashion by the use of our general theorem.

It is worth mentioning two of the limitations of the present theory under which these results have been obtained: (i) orthogonality condition; and (ii) relaxed free boundary conditions. The orthogonality condition makes it possible to carry out a detailed analysis of the fluid flows in and around hybrid droplets. One of the advantages of this assumption is that it allows us to avoid the use of toroidal coordinates to construct solutions of these problems which is very tedious and cumbersome. It is hoped that the technique presented here can be applied for the case when the two spheres intersect at a contact angle π/n, n an integer & >2. In such situations, the successive reflections will increase with increasing n adding more number of terms to the general expressions for the flow fields. However, in the general case of arbitrary contact angles, the problem has to be solved by the use of conical functions in toroidal coordinates. It would be certainly interesting to analyze the effect of contact angle on the flow fields and drag. But the possibility of solving the problem with arbitrary contact angle in the case of singularity driven flows yet remains to be explored.

The relaxed free boundary conditions (the normal stress imbalance on the free surface of the large sphere as well as the tangential stress continuity across the

bubble–liquid surface) are redundant for the limiting case of vapor–solid configuration when this free boundary (i.e., boundary of the sphere S_b in Fig. 1) is not a free boundary and the solutions perfectly make sense. In fact, one does observe in nature bubbles attached to solid fixed boundaries. Because of this, it is very likely that solutions and various flow features reported here for the vapor–liquid case will hold in a qualitative sense when the viscosity of the liquid in the drop is very high. In other cases, when the viscosity is moderate but within Stokes regime, perhaps these bubbles and associated flow features can be observed under controlled experiments as discussed in the text.

Finally, it is worth mentioning that documentation of these solutions, associated theory, and their behavior in parameter space for various underlying axisymmetric flows in this paper will hopefully lead to some further insight, novel experiments, and resolution of some of the shortcomings of the theory as mentioned above.

Acknowledgements

The authors are grateful to the reviewers for their constructive comments and suggestions.

References

[1] H. Brenner, The Stokes resistance of an arbitrary particle-V. Symbolic operator representation of intrinsic resistance, Chem. Eng. Sci. 21 (1966) 97–109.
[2] E.J. Hinch, L.G. Leal, The effect of Brownian motion on the rheological properties of a suspension of non-spherical particles, J. Fluid Mech. 52 (1972) 683–712.
[3] E. Evans, D. Needham, Attraction between lipid bilayer membranes in concentrated solutions of non-adsorbing polymers: comparison of mean-field theory with measurements of adhesion energy, Macromolecules 21 (1988) 1822–1831.
[4] E. Evans, D.J. Klingenberg, W. Rawicz, F. Szoka, Interactions between polymer-grafted membranes in concentrated solutions of free polymer, Langmuir 12 (1996) 3031–3037.
[5] R.E. Johnson, S.S. Sadhal, Fluid mechanics of compound multiphase drops and bubbles, Ann. Rev. Fluid Mech. 17 (1985) 289–320.
[6] S.S. Sadhal, P.S. Ayyaswamy, J.N. Chung, Transport Phenomena with Drops and Bubbles, Springer, New York, 1997.
[7] T.B. Jones, Effective dipole moment of conducting intersecting spheres, J. Appl. Phys. 62 (1987) 362–365.
[8] A.V. Radchik, A.V. Paley, G.B. Smith, A.V. Vagov, Polarization and resonant absorption in intersecting cylinders and spheres, J. Appl. Phys. 76 (1994) 4827–4835.
[9] U. Zimmermann, J. Vienken, Electric field-induced cell-to-cell fusion, J. Memb. Biol. 67 (1982) 165–182.
[10] S.T. Vuong, S.S. Sadhal, Growth and translation of a liquid–vapor compound drop in second liquid, Part 1. Fluid Mechanics, J. Fluid Mech. 209 (1987) 617–637.
[11] D. Palaniappan, S. Kim, Analytic solutions for Stokes flow past a partially encapsulated droplet, Phys. Fluids A9 (5) (1997) 1218–1221.
[12] D. Palaniappan, Prabir Daripa, Compound droplet in extensional and paraboloidal flows, Phys. Fluids 12 (10) (2000) 2377–2385.
[13] H.A. Lorentz, A general theorem concerning the motion of a viscous fluid and a few consequences derived from it, Verst. kon. Akad. Wet. Ams. 5 (1897) 168.

[14] A.T. Chwang, T.Y. Wu, Hydromechanics of low Reynolds-number flow. Part 2. Singularity method for Stokes flow, J. Fluid Mech. 67 (1975) 787–815.
[15] S. Kim, S.J. Karrila, Microhydrodynamics: Principles and Selected Applications, Butterwort-Heinemann, Boston, 1991.
[16] C. Pozrikidis, Boundary Integral and Singularity Methods for Linearized Viscous Flow, Cambridge University Press, Cambridge, 1992.
[17] J. Happel, H. Brenner, Low Reynolds Number Hydrodynamics, Matinus Nijhoff, The Hague, 1983.
[18] D. Palaniappan, S.D. Nigam, T. Amaranath, A theorem for a fluid sphere in Stokes flow, J. Austral. Math. Soc. Ser. B 35 (1994) 335–347.
[19] W.D. Collins, Note on a sphere theorem for the axisymmetric Stokes flow of a viscous fluid, Mathematika 5 (1958) 118–121.
[20] H. Hasimoto, Sphere theorem for axisymmetric Stokes flow, J. Phys. Soc. Japan 11 (1956) 793–796.
[21] C.W. Oseen, Hydrodynamik, Akad. Verlagsgesellschaft, Leipzig, 1927.
[22] J.J.L. Higdon, The hydrodynamics of flagellar ciliary propulsion, J. Fluid Mech. 90 (1979) 685.
[23] R. Shail, S.H. Onslow, Some asymmetric Stokes flows exterior to a spherical boundary, Mathematika 35 (1987) 233.
[24] D. Palaniappan, S.D. Nigam, T. Amaranath, R. Usha, Lamb's solution of Stokes's equations: a sphere theorem, Q. J. Mech. Appl. Math. 45 (1992) 47.
[25] Y.O. Fuentes, S. Kim, D.J. Jeffrey, Mobility functions for two unequal viscous drops in Stokes flow. I. Axisymmetric motions, Phys. Fluids 31 (1988) 2445–2455.
[26] H. Brenner, Effect of finite boundaries on the Stokes resistance of an arbitrary particle, J. Fluid Mech. 12 (1962) 35–48.
[27] G. Hetsroni, S. Haber, Flow in and around a droplet or bubble submerged in an unbounded arbitrary velocity field, Rheol Acta 9 (1970) 488–496.
[28] R.W. O'Brien, A method for the calculation of the effective transport properties of suspensions of interacting particles, J. Fluid Mech. 91 (1979) 17–39.
[29] G.K. Batchelor, J.T. Green, The determination of the bulk stress in a suspension of spherical particles to order c^2, J. Fluid Mech. 56 (1972) 401–427.
[30] H. Brenner, The Stokes resistance of an arbitrary particle, IV. Arbitrary fields of flow, Chem. Eng. Sci. 19 (1964) 703–727.
[31] J.M. Rallison, Note on the Faxen relations for a particle in Stokes flow, J. Fluid Mech. 88 (1978) 529–533.
[32] H. Brenner, S. Haber, Symbolic operator representation of generalized Faxen relation, Physico Chemical Hydrodynamics 4 (1983) 271–278.
[33] Van Dyke, An Album of Fluid Motion, Parabolic Press, Stanford, California, 1982.
[34] K. Aderogba, J.R. Blake, Action of a force near the planar surface between semi-infinite immiscible liquids at very low Reynolds numbers: Addendum, J. Bull. Aust. Math. Soc. 19 (1978) 309–318.
[35] J.R. Blake, On the generation of viscous toroidal eddies in a cylinder, J. Fluid Mech. 95 (1979) 209–222.
[36] N. Liron, J.R. Blake, Existence of viscous eddies near boundaries, J. Fluid Mech. 107 (1981) 109–129.
[37] J.R. Blake, S.R. Otto, Ciliary propulsion, chaotic filtration and a blinking stokeslet, J. Eng. Math. 30 (1996) 151–168.
[38] N. Amin, N. Riley, Streaming from a sphere due to a pulsating source, J. Fluid Mech. 210 (1990) 459–473.